

Energy-Driven Pattern Formation in Planar Dipole–Dipole Systems

Jaron Kent-Dobias

Andrew Bernoff, Advisor

May 2014



Department of Physics

Copyright © 2014 Jaron Kent-Dobias.

The author grants Harvey Mudd College the nonexclusive right to make this work available for noncommercial, educational purposes, provided that this copyright statement appears on the reproduced materials and notice is given that the copying is by permission of the author. To disseminate otherwise or to republish requires written permission from the author.

ABSTRACT

A variety of two-dimensional fluid systems, known as dipole-mediated systems, exhibit a dipole-dipole interaction between their fluid constituents. The competition of this repulsive dipolar force with the cohesive fluid forces cause these systems to form intricate and patterned structures in their boundaries. In this thesis, we show that the microscopic details of any such system are irrelevant in the macroscopic limit and contribute only to a constant offset in the system's energy. A numeric model is developed, and some important stable domain morphologies are characterized. Previously unresolved bifurcating branches are explored. Finally, by applying a random energy background to the numerics, we recover the smörgåsbord of diverse domain morphologies that are seen in experiment. We develop an empirical description of these domains and use it to demonstrate that the nondimensional parameter, Λ , which is the ratio of the line tension to the dipole-dipole density, can be extracted for any domain using only its shape.

CONTENTS

Abstract	i
Contents	iii
List of Figures	v
List of Tables	vii
Acknowledgements	ix
Notation	xi
1 Introduction	1
2 Energy Framework	5
§1. Fluid Energy	5
§2. Dipole–Dipole Energy	6
§3. Taking the Small- Δ Limit	11
§4. Background Energy	14
§5. Nondimensionalization	14
3 Analytic Results	17
§6. The Energy & Stability of Circular Domains	17
§7. The Energy & Stability of Rectangular Domains	21
4 Numerics	25
§8. Discretization	25
§9. Random Background	26
§10. Confining Well	27
§11. Lagrange’s Method	28
§12. Algorithms	31
§13. Implementation	32
5 Numeric Results	35
§14. Circle Instabilities & Bifurcations	35

§15. Stable Domains	38
§16. Domains Over Random Backgrounds	42
§17. Confined Domains	51
6 Conclusions	53
A Higher Order Energetic Moments	55
B The Gradient of the Lagrangian	59
C Modified Levenberg–Marquardt	63
Bibliography	67

LIST OF FIGURES

1.1	Examples of two-dimensional dipole-mediated systems in experiments. (a, b) Ferrofluid enclosed in a Hele-Shaw cell. Images provided by D. P. Jackson [13, 7, 22]. (c, d) 8-CB Langmuir films, or monolayers of polymer molecules, condensed into their fluid phase. Images provided by E. K. Mann [24]. (e, f) Results of the numerics which are developed in this thesis.	2
2.1	A possible fluid domain. Ω is the set of all points contained by the black line and $\partial\Omega$ is the set of points in the black line.	5
2.2	The radial distribution function for liquid argon at 85 K; data from [38]. The small fluctuations near zero are a remnant of the Fourier transform used to analyze the data.	9
3.1	A circular fluid domain.	18
3.2	The energy of a circular and rectangular domain.	23
5.1	The error $\mathcal{E}(N)$ in our numeric approximation of the critical value Λ_2 as a function of the number of boundary points used. The solid line depicts a best fit of N^{-2}	36
5.2	A circular domain alongside the first five harmonic bifurcations from a circle. (a–f) Supercritical domain structures. These shapes were taken with Λ values of (a) -1.2 , (b) -1.38 , (c) -1.52 , (d) -1.65 , (e) -1.69 , and (f) -1.77 . (g–l) Subcritical domain structures. These shapes were taken with Λ values of (g) -1.25 , (h) -1.24 , (i) -1.52 , (j) -1.67 , (k) -1.82 , and (l) -2.01	37
5.3	The perimeters of the first five harmonic bifurcations from a circular domain. The black dots represent the theoretical bifurcation points Λ_n , the solid lines denote stable numeric solutions, and the dashed lines denote unstable numeric solutions.	38
5.4	The bifurcation of the stripe/dogbone from the circle. The solid lines denote stable numeric solutions and the dashed lines denote unstable ones.	39
5.5	The energies of the first five harmonic bifurcations from a circular domain. The solid lines denote those numeric solutions, the dashed line denotes the theoretic circle energy, and the dashed line denotes the theoretic rectangle energy.	40

5.6	Representatives of (a) stripe, (b) forked, and (c) doubly forked domain morphologies at $\Lambda = -2$. These are the only stable morphologies in the absence of a random energy backdrop.	40
5.7	The asymptotic behavior of the perimeter of the three stable domain morphologies for $N = 8196$. (a) The perimeter of each morphology as a function of Λ . (b) The relative error between the perimeter of each morphology and L_{rec} , the asymptotic rectangle perimeter. . .	41
5.8	The ratios of the rectangle width w_{rec} to linear combinations of the perimeters of the (a) stripe and rectangle, (b) doubly forked, forked, and rectangle, (c) forked and stripe, (d) doubly forked and forked, and (e) doubly forked and stripe domains. Each is plotted at $N = 1200, 4096, 8192$, and the Richardson extrapolation between 4096 and 8192.	43
5.9	An example of two branches in a more complex branching domain.	45
5.10	A sampling of stable domains generated over a random energy background. Moving along the x axis corresponds to changing a_0 , the average magnitude of the background, and moving along the y axis changes Λ . Note that though all shapes are sized to fit in equally sized boxes, each has the same area in reality. All domains shown here have $N = 1200$	46
5.11	(a) The perimeters of domains generated over random energy backgrounds as a function of Λ . The solid line denotes $L_{\text{rec}}(\Lambda)$. (b) The relative error of those perimeters from the rectangle perimeter. All data is taken from shapes with $N = 1200$	47
5.12	The mean number of threefold junctions seen in annealed shapes as a function of Λ . The error bars denote standard error. Data is taken from shapes with $N = 1200$	48
5.13	The difference between the generating value Λ and the mean predicted value Λ' for domains at $N = 1200$. The error bars denote standard error.	50
5.14	Examples of domains in a confining potential. A domain is confined to a square potential and allowed to evolve with slowly varying Λ . (a-f) A domain with packing fraction $f \sim 0.2$. The values of Λ these domains were stable at are (a) -2.11 , (b) -2.25 , (c) -2.39 , (d) -2.53 , (e) -2.67 , and (f) -2.81 . (g-l) A domain with packing fraction $f \sim 0.75$. The values of Λ these domains were stable at are (g) -2.11 , (h) -2.45 , (i) -2.6 , (j) -2.77 , (k) -2.95 , and (l) -3.1 .	52

LIST OF TABLES

3.1	The exact forms of the first few constants Z_n and approximate values for associated Λ_n	21
5.1	Example domains at $N = 1200$ with generating Λ value, perimeter L , number of threefold junctions n , predicted value Λ' , and prediction error $\delta\Lambda'$	49
5.2	Example domains at $N = 8192$ with generating Λ value, perimeter L , number of threefold junctions n , predicted value Λ' , and prediction error $\delta\Lambda'$	50
5.3	Ferrofluids confined to a Hele-Shaw cell, from D. P. Jackson. Table includes dimensionless perimeter L , number of threefold junctions n , predicted value Λ' , and prediction error $\delta\Lambda'$	51

ACKNOWLEDGEMENTS

I would first and foremost like to thank my advisor, Professor Andrew J. Bernoff, for his guidance and contributions. Next, I would like to thank Professor Chad Higdon-Topaz of Macalester College and the NSF (grant DMS-1009633) for supporting my research through the summer of 2013. I would also like to thank Elizabeth Mann and David Jackson for their contribution of experimental images. Finally, I would like to thank both the Mathematics and Biology departments of Harvey Mudd College for use of their computing resources.

NOTATION

VECTORS are denoted by an arrow.

Mean values or ensemble averages of quantities are denoted by angle brackets.

Norms are denoted by double bars and absolute values by single bars.

\mathbb{R}	the real numbers
\mathbb{Z}	the integers
Ω	domain
$\partial\Omega$	domain boundary
λ	line tension
E	energy
l	perimeter
N	number of constituents OR number of boundary points
\vec{r}	position
$\vec{\mu}$	dipole moment
δ	Dirac δ -function
$\rho_N^{(2)}$	2-particle density
$g_N^{(2)}$	pair distribution function
g	radial distribution function
μ	dipole density
A	domain area
$R \equiv \sqrt{A/\pi}$	domain characteristic radius
$F \equiv E/\mu^2 R$	dimensionless energy
$L \equiv l/R$	dimensionless perimeter
$\vec{q} \equiv \vec{r}/R$	dimensionless position
$\Lambda \equiv \frac{\lambda}{\mu^2} - \log \frac{R}{\Delta}$	dimensionless parameter
L_{rec}	rectangle perimeter
w_{rec}	rectangle width

CHAPTER I
INTRODUCTION

There is a diverse class of systems in two dimensions which are principally fluid-like, but also exhibit a long-range interaction between constituent particles. In this thesis, we will examine systems for which this long-range interaction is due to dipole–dipole coupling. We will henceforth refer to any two-dimensional fluid system with a dipole–dipole interaction between its particles as a *dipole-mediated system*. As a fluid, any dipole-mediated system is subject to strong cohesive forces which manifest as an interfacial tension, while the dipole–dipole interaction causes a long-range repulsion between its fluid particles. The competition between these forces leads to the formation of intricate and patterned morphological phases in the boundaries of these systems. When in bulk, for instance, they can form labyrinths or foams, and these phases are well studied. When isolated, the boundaries of dipole-mediated systems form complex branching structures.

A great many of these systems exist in nature and are studied by researchers experimentally. Two key examples are Langmuir films and ferrofluids confined to a Hele-Shaw cell. Langmuir films are monolayers of polymer molecules deposited atop a fluid substrate that have a liquid phase and experience dipole–dipole interactions via their molecular dipole moments. Ferrofluids are ordinary liquids that have small particles of ferromagnetic material suspended in them, and in a Hele-Shaw cell such a fluid is confined between glass plates. Once subjected to an external magnetic field, the mean alignment of the ferromagnets is in the direction of the field and the ferromagnetic particles repel each other on average. Examples of each of these can be found in Fig. 1.1. Other such systems include different types of polymer layers, such as those found in vesicles and cell membranes, and in the formation of block copolymer or magnetic garnet films [32]. These systems and others are reviewed in [31]. More examples of research on pattern formation in ferrofluids can be found in [7, 10, 11, 30], and in Langmuir films in [20, 5, 23, 27, 36].

In this thesis, we develop a new way for describing the energy of arbitrary dipole-mediated systems. We demonstrate that the microscopic details of such a system are irrelevant in the macroscopic limit, and any fluid system with a few general properties can be well described by our construction. The energy expression we produce is particularly useful because it also separates out all the system parameters from the problem. In the end, the energy depends only on a single parameter, Λ , and the shape of the system’s boundary. We confirm several known analytic calculations using our energy formalism to ensure its

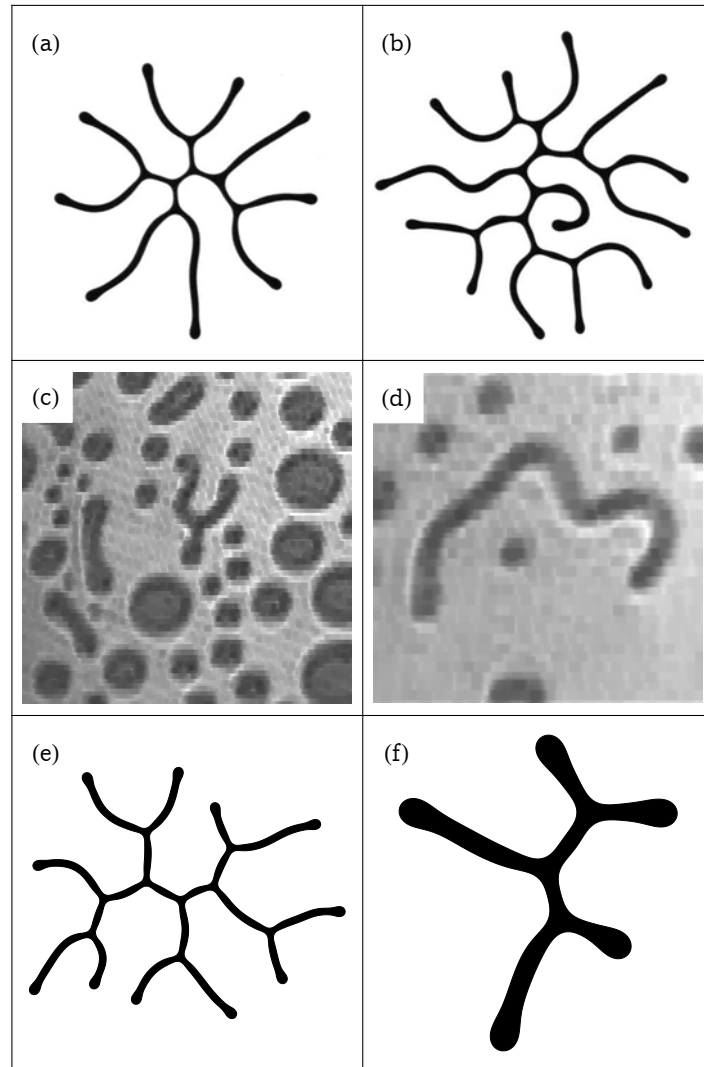


Figure 1.1: Examples of two-dimensional dipole-mediated systems in experiments. (a, b) Ferrofluid enclosed in a Hele-Shaw cell. Images provided by D. P. Jackson [13, 7, 22]. (c, d) 8-CB Langmuir films, or monolayers of polymer molecules, condensed into their fluid phase. Images provided by E. K. Mann [24]. (e, f) Results of the numerics which are developed in this thesis.

consistency.

Besides the elegance of such a description, reducing the model to a single parameter allows us to build a powerful numeric model of dipole-mediated systems. We use C++ to simulate growth and pattern formation in these systems via energy minimization routines. This is where our approach diverges from that of many others, who have predominantly modelled these systems using dynamic simulation [1, 7, 16, 19, 23, 34]. We are able to use this numeric system to trace many heretofore unknown solution branches and resolve precisely for the first time a well-studied one, the dogbone. The few stable solutions we find look very much like long rectangles with altered ends, and we use a simple model involving the exact behavior of a rectangular domain to describe their growth. However, neither the stable nor unstable solution branches we find reproduce the intricacy, asymmetry, and branching found in experimental systems.

We postulate that the lack of such structure is due to the unrealistic homogeneity that comes with simulating isolated domains. One could imagine that in experiment, small inhomogeneities in the substrate lead to a small random energy landscape which, in turn, can stabilize metastable domains. After implementing a random energy background in our numeric system to model this idea, we find that the desired features emerge with even modest levels of background. Examples of our numeric results over a random background can be seen in Fig. 1.1(e-f). Moreover, we find that the simple model we developed for describing the growth of the stable solution branches continues to work well for describing the growth of domains on the random energy background and is largely independent of the nature of that background. This is perhaps the most important result of this thesis: using a simple empirical model, one can use only the shape of a dipole-mediated domain at equilibrium to extract the defining parameter Λ . Using this method, one could use a series of experiments to find the values of the physical parameters which compose Λ , again using only pictures of the system being studied.

Finally, we also produce a numeric system for studying domains confined in a finite potential well. This sort of domain is important, because most experiments in systems such as Langmuir films do not typically study isolated domains, but rather domains in a confined bulk. We verify that the system we develop works well, and even show that labyrinthine patterns result. Extension of this research into confined domains is an obvious next step.

CHAPTER II
ENERGY FRAMEWORK

§1. Fluid Energy

In general, we are interested in finding the energy associated with arbitrary static geometric configurations of a two-dimensional liquid phase under constant external pressure. We will assume that the system at hand is in a regime with binary phases, so that the region of space containing the liquid phase of interest is sharply defined. Upon choosing a system of units, points of physical space naturally correspond to vectors in \mathbb{R}^2 . Denote by $\Omega \subset \mathbb{R}^2$ the set of vectors corresponding to points within the region occupied by the liquid phase of interest. In order for this description to make physical sense, Ω must be compact, and thus it is sensible to refer to the boundary of Ω , which we will denote by $\partial\Omega$. See, for instance, Fig. 2.1.

In three dimensions, liquids are subject to a surface tension. In fact, surface tension is but one manifestation of a much more general thermodynamic phenomenon: interfacial tension [21, page 517]. The interfacial tension associated with some phase boundary is defined to be the energy per unit boundary of the interface, and is always positive. When a phase exists in three dimensions, its boundary is an area. Ergo, surface tension is the energy per unit area of interface. However, in two dimensions, the interface is one-dimensional and the interfacial tension is the energy per unit length of interface. We will henceforth refer to this as the *line tension* of a domain, denoted by λ . The line tension is a property which can be easily determined experimentally for most fluids in

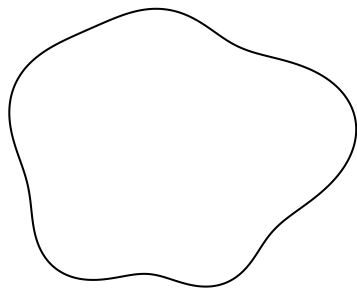


Figure 2.1: A possible fluid domain. Ω is the set of all points contained by the black line and $\partial\Omega$ is the set of points in the black line.

two dimensions; see [37] or [1] for examples of this in Langmuir films. Given the line tension λ , we can write the energy E as

$$E = \lambda l = \lambda \oint_{\partial\Omega} ds$$

Here we have simply defined the perimeter l of a region in the usual way: as the length of the region's boundary (which, in turn, is the length of its phase interface).

The astute reader will have already remembered a more familiar lesson from thermodynamics: that isobaric macroscopic systems also have an energy proportional to their spatial extent. In three dimensions, the proportionality constant between volume and energy is the pressure. Such an energy also exists for two dimensional systems, now proportional to the area of the system, with yet another constant of proportionality analogous to pressure. However, we will restrict ourselves solely to incompressible fluids. Therefore, we can presuppose that the domain has an area A , and any change of geometric configuration will also leave this area, and hence the energy associated with it, constant. If one wishes to do a similar analysis on a compressible phase, one must consider this term, but we will henceforth neglect it as a constant contribution to the energy.

It follows that, for an otherwise featureless, two-dimensional static fluid domain, the energy is given by $E = \lambda l$. A thermodynamically stable domain will minimize this energy, and therefore minimize its perimeter. The minimum perimeter of a simply connected compact region is known from the isoperimetric theorem to be a circle [8, page 33]. Thus, if Ω is simply connected, its only stable configuration is a circle. This should not be particularly surprising; after all, droplets in three dimensions naturally form spheres, which are surface area minimizers, just as circles are perimeter minimizers.

§2. Dipole–Dipole Energy

We saw in the previous section that there is only one stable configuration for a basic fluid in two dimensions: the circle. The problem becomes considerably more interesting (and difficult!) upon the addition of long-range intermolecular forces. In particular, we suppose that the particles in our fluid exhibit a dipole–dipole interaction. If the position of the i th dipole is \vec{r}_i and its dipole moment is $\vec{\mu}_i$, then the total dipole–dipole energy of the domain is

$$E_{\text{dip}} = \frac{1}{2} \sum_{i=1}^N \sum_{\substack{j=1 \\ j \neq i}}^N \frac{\vec{\mu}_i \cdot \vec{\mu}_j}{\|\vec{r}_i - \vec{r}_j\|^3}$$

We wish to transition this double sum into an integral over the area of the domain. This transition can be done exactly by simply writing

$$E_{\text{dip}} = \frac{1}{2} \sum_{i=1}^N \sum_{\substack{j=1 \\ j \neq i}}^N \vec{\mu}_i \cdot \vec{\mu}_j \iint_{\Omega} \iint_{\Omega} \frac{\delta(\vec{r} - \vec{r}_i) \delta(\vec{r}' - \vec{r}_j)}{\|\vec{r} - \vec{r}'\|^3} dA' dA$$

Since the domain in question is at thermal equilibrium, the positions of the dipoles inside it will be dynamic, causing the energy to fluctuate slightly over their motion. However, in the thermodynamic limit, these fluctuations vanish and the energy is very reliably constant. Therefore, the quantity we are actually interested in is the ensemble average of the energy, or

$$E_{\text{dip}} = \frac{1}{2} \left\langle \sum_{i=1}^N \sum_{\substack{j=1 \\ j \neq i}}^N \vec{\mu}_i \cdot \vec{\mu}_j \iint_{\Omega} \iint_{\Omega} \frac{\delta(\vec{r} - \vec{r}_i) \delta(\vec{r}' - \vec{r}_j)}{\|\vec{r} - \vec{r}'\|^3} dA' dA \right\rangle$$

We now make a simplifying assumption: that the orientation of the dipoles relative to the plane of the domain is approximately constant (or, at least, averages to a constant over length scales much smaller than the domain). This assumption is reasonable for many systems. For instance, in many varieties of Langmuir film, the molecular orientation is very close to constant and, when not, the distribution of orientations is not ordered [9, 14, 39, 35]. The same approximation is also commonly used in the literature concerning the study of ferrofluids confined to a Hele-Shaw cell, which, as fluids, do not sustain large-scale magnetic ordering and so are well-approximated this way [19, 22].

In this case, it is reasonable to pull the dipole moment dot product out of the double sum and replace it with an average dipole dot product over all particles, or

$$E_{\text{dip}} \simeq \frac{1}{2} \left\langle \langle \vec{\mu}_i \cdot \vec{\mu}_j \rangle_{ij} \sum_{i=1}^N \sum_{\substack{j=1 \\ j \neq i}}^N \iint_{\Omega} \iint_{\Omega} \frac{\delta(\vec{r} - \vec{r}_i) \delta(\vec{r}' - \vec{r}_j)}{\|\vec{r} - \vec{r}'\|^3} dA' dA \right\rangle$$

Here, we have used the notation

$$\langle f(i, j) \rangle_{ij} \equiv \sum_{i=1}^N \sum_{\substack{j=1 \\ j \neq i}}^N \frac{f(i, j)}{N^2}$$

to denote the particle average of a function f of the indices i and j . This average will, of course, also become constant in the thermodynamic limit, so

that it may be removed from the ensemble average, yielding

$$\begin{aligned}
E_{\text{dip}} &= \frac{1}{2} \langle \vec{\mu}_i \cdot \vec{\mu}_j \rangle_{ij} \left\langle \sum_{i=1}^N \sum_{\substack{j=1 \\ j \neq i}}^N \iint_{\Omega} \iint_{\Omega} \frac{\delta(\vec{r} - \vec{r}_i) \delta(\vec{r}' - \vec{r}_j)}{\|\vec{r} - \vec{r}'\|^3} dA' dA \right\rangle \\
&= \frac{1}{2} \langle \vec{\mu}_i \cdot \vec{\mu}_j \rangle_{ij} \iint_{\Omega} \iint_{\Omega} \frac{\left\langle \sum_{i=1}^N \sum_{j=1, j \neq i}^N \delta(\vec{r} - \vec{r}_i) \delta(\vec{r}' - \vec{r}_j) \right\rangle}{\|\vec{r} - \vec{r}'\|^3} dA' dA
\end{aligned} \tag{2.1}$$

We now recognize the factor in the numerator of the integral in (2.1) as the *2-particle density*

$$\rho_N^{(2)}(\vec{r}, \vec{r}') = \left\langle \sum_{i=1}^N \sum_{\substack{j=1 \\ j \neq i}}^N \delta(\vec{r} - \vec{r}_i) \delta(\vec{r}' - \vec{r}_j) \right\rangle$$

The 2-particle density gives the probability distribution for finding a particle at each of the coordinates \vec{r} and \vec{r}' in the ensemble average. While somewhat esoteric, it is a widely known and studied quantity in the statistical mechanics of fluid systems. If the system under consideration is homogeneous, then $\rho_N^{(2)}$ relates to the *pair distribution function* $g_N^{(2)}$ by

$$g_N^{(2)}(\vec{r}, \vec{r}') = \frac{\rho_N^{(2)}(\vec{r}, \vec{r}')}{\rho^2}$$

where ρ is the number density of the fluid. If the system is also isotropic, then $g_N^{(2)}$ only depends on the separation $r = \|\vec{r} - \vec{r}'\|$ and not their relative orientation, and we may simply write $g_N^{(2)}(r)$, often called the *radial distribution function* [15, page 29]. The radial distribution function gives the distribution of particle centers about a given particle in the fluid.

Luckily, most fluids are both homogeneous and isotropic, and we will assume that the domain has these properties. Therefore, the dipole energy of the domain can be written simply as

$$E_{\text{dip}} = \frac{1}{2} \rho^2 \langle \vec{\mu}_i \cdot \vec{\mu}_j \rangle_{ij} \iint_{\Omega} \iint_{\Omega} \frac{g_N^{(2)}(\|\vec{r} - \vec{r}'\|)}{\|\vec{r} - \vec{r}'\|^3} dA' dA$$

For brevity, we define $\mu^2 \equiv \rho^2 \langle \vec{\mu}_i \cdot \vec{\mu}_j \rangle_{ij}$ as the *dipole density* of our domain and write $g = g_N^{(2)}$, so that the dipole energy is, more succinctly,

$$E_{\text{dip}} = \frac{\mu^2}{2} \iint_{\Omega} \iint_{\Omega} \frac{g(\|\vec{r} - \vec{r}'\|)}{\|\vec{r} - \vec{r}'\|^3} dA' dA \tag{2.2}$$

Further analysis depends on the form of the radial distribution function $g(r)$. A similar expression is used by McConnell et al. with $g(r)$ set to the Heaviside

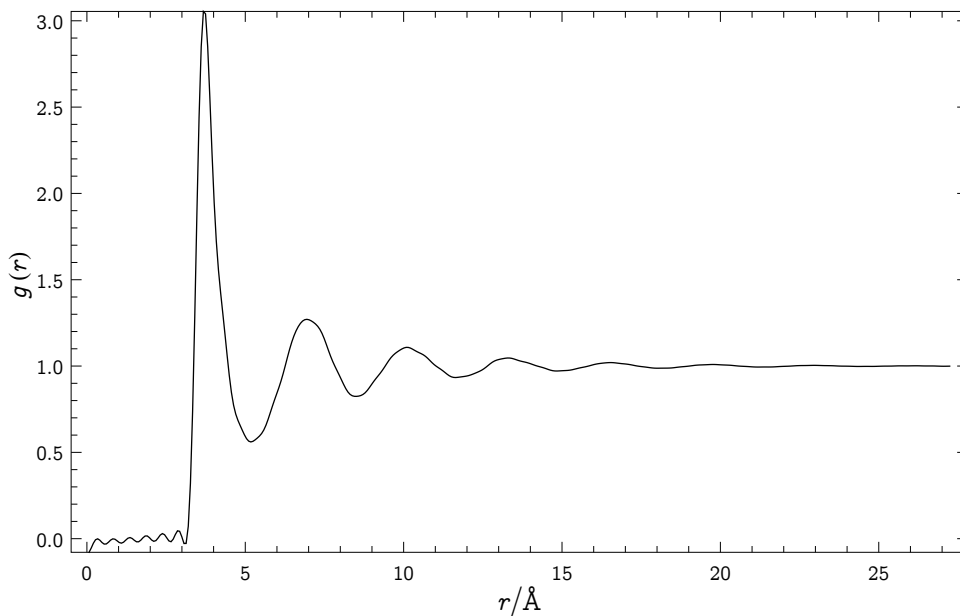


Figure 2.2: The radial distribution function for liquid argon at 85 K; data from [38]. The small fluctuations near zero are a remnant of the Fourier transform used to analyze the data.

function [28]. For any classical material, $g(0) = 0$ because two particles cannot occupy the same location. The radial distribution function must remain very near to zero for a small distance to account for the minimum spatial extent of the fluid particles. After that point, $g(r)$ may exhibit complex behavior that depends heavily on the geometry of the fluid particles. However, fluids quickly become disordered, and given our assumption of homogeneity, $g(r)$ must quickly approach one. This behavior is precisely what is seen in physical fluids; for instance, see Fig. 2.2 for a typical radial distribution function, in this case for liquid argon [38]. Choosing a functional form for $g(r)$ is a challenging theoretical problem (see [29] for a taste), and would force us to settle on a particular fluid system. In the spirit of generality, we will attempt to bring E_{dip} into quadrature without making such a choice. We simply make the following postulates about $g(r)$:

1. $\lim_{r \rightarrow 0} g(r)/r^3 < \infty$
2. $g(r)$ can be well-approximated by 1 for all $r > \Delta$.

The distance Δ will be on the order of the size of individual fluid particles, perhaps a few molecular diameters. Part of our analysis of the energy expression (2.2) will involve taking the limit of the energy with small Δ .

First, in order to make (2.2) more useful, we will convert from an area integration to a line integration. Green's theorem states, for some functions

$Q(x - x')$ and $P(y - y')$ with continuous partial derivatives in the region Ω , that

$$\iint_{\Omega} \left(\frac{\partial Q}{\partial x} - \frac{\partial P}{\partial y} \right) dA = \oint_{\partial\Omega} (P dx + Q dy)$$

Applying the theorem again, but now with respect to the primed coordinates, this expression becomes

$$\begin{aligned} & \iint_{\Omega} \iint_{\Omega} \left(\frac{\partial^2 Q}{\partial x \partial x'} + \frac{\partial^2 P}{\partial y \partial y'} \right) dA' dA = \\ & = - \iint_{\Omega} \iint_{\Omega} \left(\frac{\partial^2 Q}{\partial x^2} + \frac{\partial^2 P}{\partial y^2} \right) dA' dA = \oint_{\partial\Omega} \oint_{\partial\Omega} (P dx' dx + Q dy' dy) \end{aligned}$$

where the second step is allowed because $\partial_x Q = -\partial_{x'} Q$. If we write $Q = P = \Phi(x - x', y - y') = \Phi(\|\vec{r} - \vec{r}'\|)$, this statement becomes

$$- \iint_{\Omega} \iint_{\Omega} \nabla^2 \Phi(\|\vec{r} - \vec{r}'\|) dA' dA = \oint_{\partial\Omega} \oint_{\partial\Omega} \Phi(\|\vec{r} - \vec{r}'\|) (\hat{n} \cdot \hat{n}') ds' ds$$

where \hat{n} is the unit normal to the parameterization of the boundary $\vec{r}(s)$. Therefore, if we define a function $\Phi(r)$ such that $\nabla^2 \Phi(r) = g(r)/r^3$, the dipole energy in (2.2) can be rewritten as

$$E_{\text{dip}} = -\frac{\mu^2}{2} \oint_{\partial\Omega} \oint_{\partial\Omega} \Phi(\|\vec{r} - \vec{r}'\|) (\hat{n} \cdot \hat{n}') ds' ds \quad (2.3)$$

Recall that the radial Laplacian in polar coordinates is given by $\frac{1}{r} \partial_r r \partial_r$. We can write a formal solution for $\Phi(r)$ by inverting this and integrating by parts. This process yields

$$\begin{aligned} \Phi(r) &= \int_0^r \frac{1}{r'} \int_0^{r'} r'' \left[\frac{g(r'')}{r''^3} \right] dr'' dr' \\ &= \frac{g(r)}{r} - \int_0^r \left[\frac{g'(r')}{r'} - \frac{1}{r'} \int_0^{r'} \frac{g'(r'')}{r''} dr'' \right] dr' \end{aligned} \quad (2.4)$$

This form of the dipole energy is certainly more useful than the area integral, but it still cannot be evaluated explicitly without making a choice for the pair correlation function. We will show in the next section that this choice is largely arbitrary and results only in constant shifts to the effective line tension for the system.

It is worth discussing why we only consider a molecular pair energy that is dipolar. What about higher-order moments, which complex molecules inevitably have? The short answer is that higher-order moments contribute solely

to the line tension λ in the macroscopic limit. Therefore, the contribution of these terms to the energy expression is already accounted for by the experimental determination of the line tension. The dipole energy is different, however, because its contribution (as we shall see very explicitly) relies strongly on the large-scale structure of the domain. The longer answer, in which these facts are demonstrated in a toy system, can be found in Appendix A.

§3. Taking the Small- Δ Limit

In this section, we will make use of some techniques from asymptotic analysis to take the limit as $\Delta \rightarrow 0$ in the dipole energy expression (2.3). Note that we cannot simply do this in the naïve way by bringing $\Delta \rightarrow 0$ immediately and carrying on from there. This is because, when $\Delta \rightarrow 0$, $g(r) = 1$ for all $r > 0$, and, using (2.4), the function $\Phi(r) = 1/r$. The energy would then be

$$E_{\text{dip}} = -\frac{\mu^2}{2} \oint_{\partial\Omega} \oint_{\partial\Omega} \frac{\hat{n} \cdot \hat{n}'}{\|\vec{r} - \vec{r}'\|} ds' ds$$

which has a divergent and non-integrable integrand when $\vec{r} = \vec{r}'$. As we will show, the dependence of E_{dip} on Δ cannot completely be removed. Instead, we will do the next best thing and remove Δ dependence from the integration.

First, we explicitly parameterize the integral (2.3) by arc length, which yields

$$E_{\text{dip}} = -\frac{\mu^2}{2} \int_0^l \int_0^l \Phi(\|\vec{r}(s) - \vec{r}(s')\|) [\hat{n}(s) \cdot \hat{n}(s')] ds' ds$$

Defining $\sigma \equiv s' - s$, we can reparameterize this integral yet again so that it is in the form

$$E_{\text{dip}} = -\frac{\mu^2}{2} \int_0^l \int_{-\frac{1}{2}}^{\frac{1}{2}} \Phi(\|\vec{r}(s) - \vec{r}(s + \sigma)\|) [\hat{n}(s) \cdot \hat{n}(s + \sigma)] d\sigma ds \quad (3.1)$$

Consider some function $j(r, \Delta)$ with the following two properties:

$$\lim_{\Delta \rightarrow 0} j(r, \Delta) = \frac{1}{r} \quad J(\Delta) \equiv \frac{1}{2} \int_{-\frac{1}{2}}^{\frac{1}{2}} j(|\sigma|, \Delta) d\sigma < \infty \quad (3.2)$$

To simplify the formulae, we also define

$$\xi \equiv \|\vec{r}(s) - \vec{r}(s + \sigma)\| \quad \cos \psi \equiv \hat{n}(s) \cdot \hat{n}(s + \sigma)$$

Keep in mind that each of these expressions is an implicit function of s and σ . Given these, the energy (3.1) is

$$E_{\text{dip}} = -\frac{\mu^2}{2} \int_0^l \int_{-\frac{1}{2}}^{\frac{1}{2}} \Phi(\xi) \cos \psi d\sigma ds \quad (3.3)$$

Now we simply add and subtract $j(r, \Delta)$ from the integrand of (3.3) to find

$$\begin{aligned}
E_{\text{dip}} &= -\frac{\mu^2}{2} \int_0^l \int_{-\frac{l}{2}}^{\frac{l}{2}} [\Phi(\xi) \cos \psi - j(|\sigma|, \Delta) + j(|\sigma|, \Delta)] \, d\sigma \, ds \\
&= -\frac{\mu^2}{2} \int_0^l \int_{-\frac{l}{2}}^{\frac{l}{2}} [\Phi(\xi) \cos \psi - j(|\sigma|, \Delta)] \, d\sigma \, ds - \frac{\mu^2}{2} \int_0^l \int_{-\frac{l}{2}}^{\frac{l}{2}} j(|\sigma|, \Delta) \, d\sigma \, ds \\
&= -\frac{\mu^2}{2} \int_0^l \int_{-\frac{l}{2}}^{\frac{l}{2}} [\Phi(\xi) \cos \psi - j(|\sigma|, \Delta)] \, d\sigma \, ds - \mu^2 \int_0^l J(\Delta) \, ds \\
&= -\frac{\mu^2}{2} \int_0^l \int_{-\frac{l}{2}}^{\frac{l}{2}} [\Phi(\xi) \cos \psi - j(|\sigma|, \Delta)] \, d\sigma \, ds - \mu^2 J(\Delta) l \quad (3.4)
\end{aligned}$$

We can now take the limit as $\Delta \rightarrow 0$ of the remaining integrand. The function $j(r, \Delta)$ behaves as described in (3.2). Since, as $\Delta \rightarrow 0$, $g(r) = 1$ for all $r > 0$, it follows that $g'(r) = 0$ for $r > 0$ as well, and (2.4) yields

$$\lim_{\Delta \rightarrow 0} \Phi(r) = \frac{1}{r}$$

Therefore, when we take $\Delta \rightarrow 0$ in the integrand of (3.4), we find, returning to our original notation, that

$$E_{\text{dip}} \simeq -\frac{\mu^2}{2} \int_0^l \int_{-\frac{l}{2}}^{\frac{l}{2}} \left[\frac{\hat{n}(s) \cdot \hat{n}(s + \sigma)}{\|\vec{r}(s) - \vec{r}(s + \sigma)\|} - \frac{1}{|\sigma|} \right] \, d\sigma \, ds - \mu^2 J(\Delta) l \quad (3.5)$$

This integral, which without the addition of $j(r, \Delta)$ would be singular, does converge. This can be seen by examining the behavior of the integrand where it is possibly divergent, or when $\sigma = 0$. Using elementary differential geometry, the Taylor expansion of $\vec{r}(s + \sigma)$ about $\sigma = 0$ is

$$\begin{aligned}
\vec{r}(s + \sigma) &= \vec{r}(s) + \sigma \left. \frac{\partial \vec{r}(s + \sigma)}{\partial \sigma} \right|_{\sigma=0} + \frac{\sigma^2}{2} \left. \frac{\partial^2 \vec{r}(s + \sigma)}{\partial \sigma^2} \right|_{\sigma=0} + \mathcal{O}(\sigma^3) \\
&= \vec{r}(s) + \sigma \hat{t}(s) + \frac{\sigma^2}{2} \kappa(s) \hat{n}(s) + \mathcal{O}(\sigma^3)
\end{aligned}$$

where $\kappa(s)$ is the curvature of the boundary at $\vec{r}(s)$ [8]. The expansion of the normed factor in the denominator of the integrand of (3.5) therefore comes to

$$\|\vec{r}(s) - \vec{r}(s + \sigma)\| = \|\sigma \hat{t}(s) + \frac{\sigma^2}{2} \kappa(s) \hat{n}(s) + \mathcal{O}(\sigma^3)\| = |\sigma| + \mathcal{O}(\sigma^3) \quad (3.6)$$

The tangent to the boundary has a similar expansion, given by

$$\hat{t}(s + \sigma) = \hat{t}(s) + \sigma \kappa(s) \hat{n}(s) + \mathcal{O}(\sigma^2)$$

It follows that the dot product of normals, which is equivalent to the dot product of tangents, is given by

$$\begin{aligned}
\hat{n}(s) \cdot \hat{n}(s + \sigma) &= \hat{t}(s) \cdot \hat{t}(s + \sigma) = \hat{t}(s) \cdot [\hat{t}(s) + \sigma \kappa(s) \hat{n}(s) + \mathcal{O}(\sigma^2)] \\
&= 1 + \mathcal{O}(\sigma^2) \quad (3.7)
\end{aligned}$$

Thus, upon substitution of the vector expansions (3.6) and (3.7), the asymptotic behavior of the integrand of (3.5) around small σ is

$$\frac{\hat{n}(s) \cdot \hat{n}(s + \sigma)}{\|\vec{r}(s) - \vec{r}(s + \sigma)\|} - \frac{1}{|\sigma|} = \frac{1 + \mathcal{O}(\sigma^2)}{|\sigma| + \mathcal{O}(\sigma^3)} - \frac{1}{|\sigma|} = \mathcal{O}(\sigma^2)$$

and hence is not divergent as $\sigma \rightarrow 0$.

Therefore, we have been able to completely remove the dependence on $g(r)$ from the integration. This may seem worrisome, since $g(r)$ implicitly contained information about the microscopic parameters of the system, like the length scale Δ . This parameter still enters the energy, but now through the function $J(\Delta)$, which we have yet to choose. For instance, we could choose

$$j(r, \Delta) = \frac{\Theta(r - \frac{\Delta}{2}) + \Theta(-r - \frac{\Delta}{2})}{r}$$

where Θ is the Heaviside function. This clearly fulfills the first condition of (3.2), and it follows immediately that

$$J(\Delta) = \frac{1}{2} \int_{-\frac{l}{2}}^{\frac{l}{2}} j(|\sigma|, \Delta) d\sigma = \frac{1}{2} \left(\int_{-\frac{l}{2}}^{-\frac{\Delta}{2}} \frac{1}{|\sigma|} d\sigma + \int_{\frac{\Delta}{2}}^{\frac{l}{2}} \frac{1}{|\sigma|} d\sigma \right) = \log \frac{l}{\Delta}$$

Using this, the dipole energy would become

$$E_{\text{dip}} = -\frac{\mu^2}{2} \int_0^l \int_{-\frac{l}{2}}^{\frac{l}{2}} \left[\frac{\hat{n}(s) \cdot \hat{n}(s + \sigma)}{\|\vec{r}(s) - \vec{r}(s + \sigma)\|} - \frac{1}{|\sigma|} \right] d\sigma ds - \mu^2 l \log \frac{l}{\Delta}$$

This choice of $j(r, \Delta)$ is motivated mostly by its simplicity. Many other options are available, though for consistency with the small Δ approximation one usually must then expand $J(\Delta)$ around $\frac{\Delta}{l} = 0$ and use the highest-order term. In any such case, given the asymptotic behavior of $j(r, \Delta)$ as defined above, the highest-order term will be proportional to $\log \frac{l}{\Delta}$, and the particular choice of j will only modify the proportionality constant. It is natural to ask how much error is introduced by making the approximation $\Delta \rightarrow 0$ in the integrand of (3.5). In general, $g(r)$ can be assumed to be a C^∞ function, and so it will have a Taylor expansion about $r = 0$. The error contributed by the n th order term $g_n(r) \equiv g^{(n)}(0)r^n/n!$ is given by

$$\begin{aligned} \mathcal{E}_n &= \frac{\mu^2}{2} \int_0^l \int_{-\frac{l}{2}}^{\frac{l}{2}} \left\{ \frac{g_n(\sigma)}{\sigma} + \int_0^\sigma \left[\frac{g'_n(r')}{r'} - \frac{1}{r'} \int_0^{r'} \frac{g'_n(r'')}{r''} dr'' \right] dr' \right\} d\sigma ds \\ &= \mu^2 g^{(n)}(0) l [\Delta^n - (-\Delta)^n] \frac{2n(n-2)+1}{2(n-1)^2 n!} \propto \mu^2 g^{(n)}(0) l \Delta^n \end{aligned}$$

The error contribution is of order Δ^n and is only nonzero for odd n .

§4. Background Energy

Later, we will also want to subject our domain to a static external spatial potential. In general, we can write an energy per unit area of domain $u(\vec{r})$. Then, the total energy of the domain due to this background will be given by

$$E_{\text{back}} = \iint_{\Omega} u(\vec{r}) \, dA$$

We can apply Green's theorem precisely as we did before. If $\vec{\Psi}$ is a function such that $\vec{\nabla} \cdot \vec{\Psi}(\vec{r}) = u(\vec{r})$, then we may write

$$E_{\text{back}} = \oint_{\partial\Omega} \vec{\Psi}(\vec{r}) \cdot \hat{n} \, ds \quad (4.1)$$

We cannot produce a more explicit form for this background until we specify the function $u(\vec{r})$. We will do this when it becomes relevant in the numerics chapter. Unless explicitly stated otherwise, one can assume that $u(\vec{r}) = 0$ in this thesis.

§5. Nondimensionalization

The total energy of a dipole-mediated domain can now be written as

$$\begin{aligned} E &= \lambda l + E_{\text{dip}} + E_{\text{back}} \\ &= \lambda l - \frac{\mu^2}{2} \oint_{\partial\Omega} \int_{-\frac{l}{2}}^{\frac{l}{2}} \left[\frac{\hat{n}(s) \cdot \hat{n}(s + \sigma)}{\|\vec{r}(s) - \vec{r}(s + \sigma)\|} - \frac{1}{|\sigma|} \right] \, d\sigma \, ds - \mu^2 l \log \frac{l}{\Delta} + \\ &\quad + \oint_{\partial\Omega} \vec{\Psi}(\vec{r}) \cdot \hat{n} \, ds \quad (5.1) \end{aligned}$$

A similar expression for the energy of Langmuir films in particular has been used previously by McConnell and de Koker, who were able to make an identical separation of the quantity Δ from the integration in the boundary-integration form [26, 4]. However, in that case the separation was made using a particular form of $g(r)$ chosen specifically to describe Langmuir films. Our approach is more powerful in that it works for any of a wide variety of dipolar fluid systems. In addition to this energy expression, the systems we study are also subject to a constant area constant, which can be expressed explicitly by

$$A = \iint_{\Omega} dA = \frac{1}{2} \oint_{\partial\Omega} \|\vec{r} \times \frac{\partial \vec{r}}{\partial s}\| \, ds$$

The expression (5.1) can be framed in a far simpler way by defining dimensionless versions of the physical quantities involved. First, we define $R \equiv$

$\sqrt{A/\pi}$ as the characteristic radius of the domain. This distance is a length scale for the domain, and gives the actual radius if the domain is circular. Using this, we then proceed to define

$$F \equiv \frac{E}{\mu^2 R} \quad L \equiv \frac{l}{R} \quad \vec{\varrho} \equiv \frac{\vec{r}}{R} \quad \Lambda \equiv \frac{\lambda}{\mu^2} - \log \frac{R}{\Delta} \quad \vec{\Pi} \equiv \frac{\vec{\Psi}}{\mu^2 R}$$

Upon substitution of these quantities into (5.1), we find that

$$F = \Lambda L - \frac{1}{2} \oint_{\partial\Omega} \int_{-\frac{l}{2}}^{\frac{l}{2}} \left[\frac{\hat{n}(s) \cdot \hat{n}(s + \sigma)}{\|\vec{\varrho}(s) - \vec{\varrho}(s + \sigma)\|} - \frac{1}{|\sigma|} \right] d\sigma ds - L \log L + \oint_{\partial\Omega} \vec{\Pi}(\vec{r}) \cdot \hat{n} ds \quad (5.2)$$

This expression, along with the now dimensionless area constraint

$$\pi = \frac{1}{2} \oint_{\partial\Omega} \|\vec{\rho} \times \frac{\partial \vec{\rho}}{\partial s}\| ds$$

fully describe the system at hand. This expression only depends on one parameter, Λ , and on the shape of the domain boundary $\partial\Omega$. The constant Λ is an effective line tension that is the ratio of the real line tension to the dipole density, shifted by a constant which depends on the scale of the system. This means that, for isolated shapes, the parameter space of the system is only one dimensional!

We have now brought our description of the dipole-mediated system to an exceedingly simple form. The separation of the parameter Δ from its implicit dependence within the integrand will prove invaluable when we attempt to numerically simulate these domains. Previous researchers have approached the modelling problem without making such a reduction, but were subsequently forced to choose Δ such that their numerics were tractable. For instance, Heinig, Helseth, and Fischer set $\Delta = 1.5 \mu\text{m}$ in simulations of Langmuir films using dynamic evolution, which is arguably an unphysical value [16]. The encapsulation of this parameter into the new dimensionless parameter Λ outside the integral is the main result of this energy chapter.

It is important to note that, for shapes confined to some finite region, a second parameter also enters, the *packing fraction* f . Additional parameters will also arise when we introduce a random energy background in Chapter 4, like the characteristic amplitude a_0 and wavenumber k_0 of the energetic noise. We will discuss these other parameters more later. For now, as we study isolated domains, the fact that the system is described by only Λ will considerably ease our numerical analysis.

CHAPTER III
ANALYTIC RESULTS

Unfortunately, there are very few domain geometries for which the energy (5.2) can be evaluated exactly. However, a few tractable and insightful examples do exist. In this chapter, we will evaluate the energy and stability of two simple domain geometries: the circle and the rectangle. As we will see in subsequent chapters, these two geometries are of special importance in the study of dipole-mediated systems, and the results from this chapter will play a key role in testing the accuracy of our numerics and in providing powerful models of more complicated domain morphologies.

§6. The Energy & Stability of Circular Domains

The circular domain is important to the study of dipolar fluids because it is so commonly found. We saw why in §1: lacking other energetic terms, an isolated and simply connected fluid domain will have a circle as its energy minimum, as circles minimize a domain's perimeter. This corresponds to a regime where the parameter Λ is large, and once Λ is sufficiently large, the energy minimizer remains a circle for all larger Λ . In this section, we will answer two important questions about circular domains. First, we will find the energy of a circular domain explicitly. Then, we will determine when a circular domain becomes unstable to perturbations of various orders. These calculations have been made already by a number of authors, first by McConnell [25] and later by Goldstein et al. [13], Deutch et al. [6], and Otto [30]. Dynamic analyses have also been done of the circular instabilities [33].

Given our nondimensionalization, the dimensionless area A/R^2 must equal π . Therefore, the circular domain must have unit radius and its boundary can be parameterized by arc length using the radius vector

$$\vec{\rho}(s) = \cos s \hat{x} + \sin s \hat{y} \tag{6.1}$$

Since s is the arc-length of a unit circle, it also corresponds to the angle about the circle. Therefore, $L = 2\pi$, so that (5.2) becomes

$$F_o = \Lambda 2\pi - \frac{1}{2} \oint_{\partial\Omega} \int_{-\pi}^{\pi} \left[\frac{\hat{n}(s) \cdot \hat{n}(s + \sigma)}{\|\vec{\rho}(s) - \vec{\rho}(s + \sigma)\|} - \frac{1}{|\sigma|} \right] d\sigma ds - 2\pi \log(2\pi) \tag{6.2}$$

Here σ is the angle between $\vec{\rho}(s)$ and $\vec{\rho}(s + \sigma)$. This geometry is illustrated in Fig. 3.1. Since $\vec{\rho}$ is always perpendicular to the boundary of the circle and of

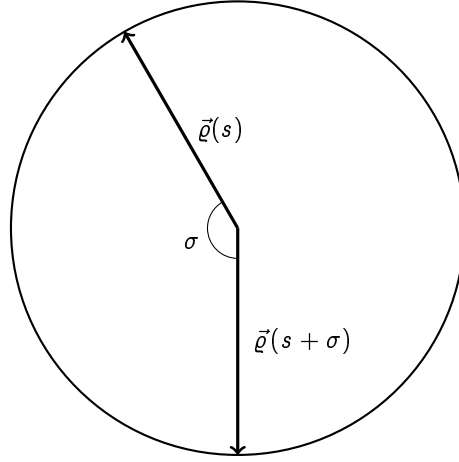


Figure 3.1: A circular fluid domain.

unit length, it follows that

$$\hat{n}(s) \cdot \hat{n}(s + \sigma) = \vec{\rho}(s) \cdot \vec{\rho}(s + \sigma) = \cos \sigma$$

The norm of their difference also follows quickly using the law of cosines, or

$$\|\vec{\rho}(s) - \vec{\rho}(s + \sigma)\|^2 = 2 - 2 \cos \sigma = 4 \sin^2 \frac{\sigma}{2}$$

Therefore, the expression (6.2) becomes

$$F_o = \Lambda 2\pi - \frac{1}{2} \oint_{\partial\Omega} \int_{-\pi}^{\pi} \left[\frac{\cos \sigma}{2|\sin \frac{\sigma}{2}|} - \frac{1}{|\sigma|} \right] d\sigma ds - 2\pi \log(2\pi)$$

The integration in s may be carried out immediately to yield a factor of the perimeter,

$$F_o = \Lambda 2\pi - \pi \int_{-\pi}^{\pi} \left[\frac{\cos \sigma}{2|\sin \frac{\sigma}{2}|} - \frac{1}{|\sigma|} \right] d\sigma - 2\pi \log(2\pi)$$

Since the integrand is symmetric in σ , we may halve the limits of integration and double the result, nullifying the absolute values and yielding

$$F_o = \Lambda 2\pi - 2\pi \int_0^{\pi} \left[\frac{\cos \sigma}{2 \sin \frac{\sigma}{2}} - \frac{1}{\sigma} \right] d\sigma - 2\pi \log(2\pi)$$

This integral has now been reduced to quadrature and can be solved using symbolic computation software or integral tables. The result is

$$F_o = \Lambda 2\pi + 2\pi \left(2 + \log \frac{\pi}{4} \right) - 2\pi \log(2\pi) = 2\pi (\Lambda + 2 - \log 8)$$

This expression for the energy of a circular domain is consistent with that found previously by McConnell [25].

The circular domain does not remain a stable shape when Λ becomes sufficiently small, however. At some point, the repulsive forces within the fluid bulk make it energetically favorable to increase the perimeter in order to stretch out the domain. This happens when the circle stops being an energy minimizer, so that small perturbations away from a circular shape cause the energy of the system to decrease. Because of the circle's natural symmetry, the resulting bifurcating shapes have broken rotational symmetry of various orders. The circle becomes unstable to perturbations of different orders at different values of Λ . We therefore wish to find the points at which a circular domain becomes unstable to harmonic perturbations to its boundary, or perturbations of the type

$$\delta \vec{\varrho}_n(\theta) = [\eta + \varepsilon \cos(n\theta)] \vec{\varrho}(\theta) \quad (6.3)$$

Here $\varepsilon \ll 1$, $n \in \mathbb{Z}^+$ and $n \geq 2$, $\varrho(\theta)$ is given by (6.1), and η is a dimensionless parameter which we will later fix to ensure that the area of the perturbed domain is constant. We will also denote by

$$\vec{\varrho}_n(\theta) = \vec{\varrho}(\theta) + \delta \vec{\varrho}_n(\theta)$$

the boundary of a perturbed circle. Note that this boundary is no longer parameterized by arc length. For each n , we hope to find Λ_n , the value of Λ at which a circular domain becomes unstable to perturbations of the type $\delta \vec{\varrho}_n$. In particular, one expects that the circular domain first becomes unstable at Λ_2 , which corresponds to the lowest-order perturbation.

In order for such a perturbation to be consistent with our energy expression from §5, it must not change the area of the domain. For a stability analysis, precision of up to quadratic order in the small parameter ε will suffice. The area of a perturbed domain is given by

$$\begin{aligned} A &= \iint_{\Omega} dA = \int_0^{2\pi} \int_0^{\varrho_n(\theta)} \varrho' d\varrho' d\theta = \int_0^{2\pi} \frac{1}{2} \varrho_n^2(\theta) d\theta \\ &= \int_0^{2\pi} \frac{1}{2} \|\vec{\varrho}(\theta) + \delta \vec{\varrho}_n(\theta)\|^2 d\theta = \pi \left(1 + 2\eta + \eta^2 + \frac{\varepsilon^2}{2} \right) \end{aligned}$$

For the area to remain the same, $A = \pi$, so that

$$\eta = \sqrt{1 - \frac{\varepsilon^2}{2}} - 1 = -\frac{\varepsilon^2}{4} + \mathcal{O}(\varepsilon^4) \quad (6.4)$$

With the addition of (6.4), (6.3) becomes

$$\delta \vec{\varrho}_n(\theta) = \left[-\frac{\varepsilon^2}{4} + \varepsilon \cos(n\theta) \right] \vec{\varrho}(\theta)$$

These perturbations now result in consistent domain areas.

To evaluate the integral in (5.2), we must parameterize this curve by arc length rather than angle. We first seek the angle along the perturbed domain is a function of arc length, or $\theta_n(s)$. By the Pythagorean theorem,

$$\begin{aligned} \frac{ds_n}{d\theta} &= \left\| \frac{\partial \vec{\rho}_n}{\partial \theta} \right\| = \sqrt{\rho_n^2 + \partial_\theta \rho_n} \\ &= 1 + \varepsilon \cos(n\theta) - \frac{\varepsilon^2}{4} \{1 + n^2 [1 - \cos(2n\theta)]\} + \mathcal{O}(\varepsilon^3) \end{aligned}$$

We can now easily find the domain's perimeter, or

$$L_n = \int_0^{2\pi} \frac{ds_n}{d\theta} d\theta = 2\pi \left[1 + \frac{\varepsilon^2}{4} (n^2 - 1) \right] + \mathcal{O}(\varepsilon^3)$$

We can also partially evaluate this integral to find the arc length as a function of angle, or

$$\begin{aligned} s_n(\theta) &= \int_0^\theta \frac{ds}{d\theta} d\theta \\ &= \theta + \frac{\varepsilon}{n} \sin(n\theta) + \frac{\varepsilon^2}{8} [2\theta(n^2 - 1) + n \sin(2n\theta)] + \mathcal{O}(\varepsilon^3) \end{aligned} \quad (6.5)$$

In order to find $\theta_n(s)$, we need to find the inverse of this expression. However, its complexity makes this prohibitive. Therefore, we will take an iterative approach in orders of the parameter ε . To zeroth order in ε , we have

$$s_n^{(0)}(\theta) = \theta$$

so that

$$\theta_n^{(0)}(s) = s$$

To first order in ε , the arc length as a function of θ is given by

$$s_n^{(1)}(\theta) = \theta + \frac{\varepsilon}{n} \sin(n\theta)$$

Once again, we invert this expression, but replace θ in higher order terms with our previous level of approximation, $\theta_n^{(0)}$. Therefore, we have

$$\theta_n^{(1)}(s) = s - \frac{\varepsilon}{n} \sin[n\theta_n^{(0)}(s)] = s - \frac{\varepsilon}{n} \sin(ns)$$

The expression (6.5) is already second order in ε . Continuing the iterative pattern and only keeping terms to second order in ε , we have

$$\begin{aligned} \theta_n^{(2)}(s) &= s - \frac{\varepsilon}{n} \sin[n\theta_n^{(1)}(s)] - \frac{\varepsilon^2}{8} \left\{ 2\theta_n^{(0)}(s)(n^2 - 1) + n \sin[2n\theta_n^{(0)}(s)] \right\} \\ &= s - \frac{\varepsilon}{n} \sin \left\{ n \left[s - \frac{\varepsilon}{n} \sin(ns) \right] \right\} - \frac{\varepsilon^2}{8} [2s(n^2 - 1) + n \sin(2ns)] \\ &= s - \frac{\varepsilon}{n} \sin(ns) - \frac{\varepsilon^2}{8} \left[2s(n^2 - 1) + n \sin(2ns) + \frac{8}{n} \sin(ns) \cos(ns) \right] + \mathcal{O}(\varepsilon^3) \end{aligned}$$

Table 3.1: The exact forms of the first few constants Z_n and approximate values for associated Λ_n .

n	Z_n	Λ_n	n	Z_n	Λ_n
2	10/3	-1.254	7	3077/693	-2.361
3	11/3	-1.587	8	864202/189189	-2.488
4	98/25	-1.841	9	1054393/225225	-2.602
5	433/105	-2.044	10	17269258/3610035	-2.704
6	47342/11025	-2.215	11	50679253/10392525	-2.797

This is sufficiently precise in ε for integration. The function $\tilde{\varrho}_n[\theta_n^{(2)}(s)]$ parameterizes the domain by arc length to second order in ε , and can be substituted into the integral (5.2), which is then reduced to quadrature and can be computed using symbolic mathematics software. Once the energy E_n of a perturbed domain is computed, the critical Λ can be found by solving $E_n(\Lambda_n) - E_o(\Lambda_n) = 0$, since, at the critical value, the energy of the perturbed domain will cross over from greater than circle energy to less than circle energy.

The resulting critical values of Λ are given by $\Lambda_n = \log 8 - Z_n$, where the first few Z_n are tabulated in Table 3.1. These are also the values of Z_n which were found by McConnell in [25] for Langmuir domains explicitly. These values also match those found by Goldstein & Jackson, who, in addition, supplied a closed form for Z_n , given by

$$Z_n = \frac{5}{2} + \frac{1}{2} \left(\frac{4n^2 - 1}{n^2 - 1} \right) \sum_{j=2}^n \frac{1}{2j - 1}$$

which coincides exactly with the values of Z_n we computed individually [13]. These instability points have also been observed to occur in experiments on Langmuir systems [12]. We will use these critical values to test the accuracy of our numerics later, as each harmonic instability can be easily found using our numeric system.

§7. The Energy & Stability of Rectangular Domains

Another important shape is the rectangle, especially in the limit of high aspect ratio. When one looks at experimental domains, the most common pattern after circle formation is stripe-like, either in the form of labyrinths or long branching arms. It seems reasonable to model the behavior of individual branches as if they were rectangles. As we will later see in our numerics, physical domains are surprisingly well modelled using rectangular domains in the limit of large Λ , and so expressions for their perimeter and energy in this limit will prove vital.

If a is the aspect ratio of the domain, then the x and y dimensions of the domain are given by $d_x = \sqrt{a\pi}$ and $d_y = \sqrt{\frac{\pi}{a}}$, respectively. The boundary of

such a rectangle parameterized by arc length is given by

$$\vec{\rho}(s) = \begin{cases} s\hat{x} & s < d_x \\ d_x\hat{x} + (s - d_x)\hat{y} & d_x < s < d_x + d_y \\ (2d_x + d_y - s)\hat{x} + d_y\hat{y} & d_x + d_y < s < 2d_x + d_y \\ (2d_x + 2d_y - s)\hat{y} & 2d_x + d_y < s < 2d_x + 2d_y \end{cases}$$

By integrating this boundary in the energy expression (5.2), we can determine the energy of this rectangle. In the limit of large a , or high aspect ratio, the energy is given by

$$F_{\text{rec}} = 2\sqrt{\pi a} \left(\Lambda - \frac{1}{2} \log \frac{\pi}{a} \right) + \mathcal{O}(a^{-1/2})$$

The domain will be stable when this energy is minimized with respect to a . The value of the aspect ratio which minimizes the energy is given by

$$a(\Lambda) = \pi e^{-2(\Lambda+1)}$$

which corresponds to a domain perimeter of

$$L_{\text{rec}}(\Lambda) = 2(d_x + d_y) = 2\pi e^{-\Lambda-1}$$

and a rectangle energy of $F_{\text{rec}}(\Lambda) = -2\pi e^{-\Lambda-1}$. Remarkably, we find that as Λ decreases, the aspect ratio of a rectangular domain grows exponentially, and as a result so does its perimeter. We also find that the minimum energy of a rectangle becomes more negative exponentially with negative Λ . This result matches what has been found previously by McConnell et. al [22] and Jackson et. al [28].

Since the energy of a rectangle decreases exponentially with decreasing negative Λ , the rectangle will eventually have lower energy than the circle. This will happen when $F_{\text{rec}}(\Lambda) = F_{\text{o}}(\Lambda)$. Though rectangles themselves will clearly not be minimizers for physical domains, the presence of stripe-like components in physical domains does suggest that at least the rectangle structure is similar to a minimizing structure. Both circle and rectangle energies are plotted in Fig. 3.2, and the intersection point is given by $\Lambda = -1.374$. Recall that the circle first becomes unstable at $\Lambda_2 = -1.254$. The fact that these two values of Λ are so similar is not a coincidence: we will show in the numeric results of Chapter 5 that the energy-minimizing shape past the circle instability is a single stripe, precisely the extension of a rectangle. Even beyond the global minimizer, stripe-like branching structures unambiguously dominate in this region.

Such a minimizing solution is not useful, however, if it becomes unstable during its evolution. In particular, we would like to find whether the long, stripe-like portion of a rectangular domain becomes unstable at some length, or rather thickness. McConnell, de Koker, & Jiang found previously that an infinite stripe becomes unstable when its width is greater than the critical

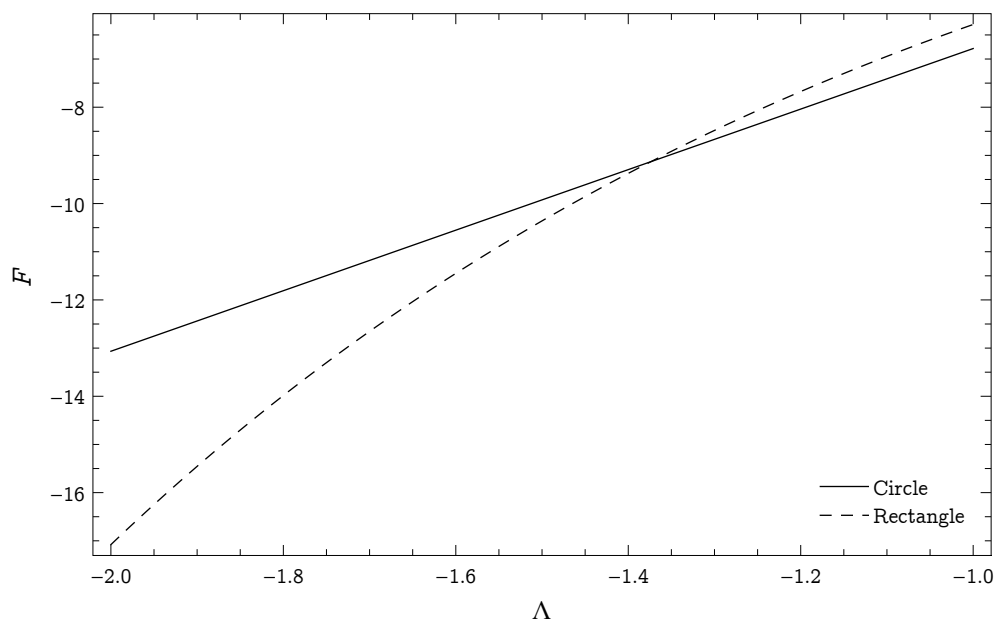


Figure 3.2: The energy of a circular and rectangular domain.

width $w_c(\Lambda) = e^{\Lambda+\gamma+2}$, where γ is Euler's constant [3]. The width is simply given by d_y , so that

$$w_{\text{rec}}(\Lambda) = d_y = e^{\Lambda+1}$$

Since $w_{\text{rec}}(\Lambda) < w_c(\Lambda)$ for all values of Λ , this theory predicts that the body of energy-minimizing rectangular or rectangle-like domains will remain stable at all values of Λ . Thus, we should expect stripe-like patterns to remain stable.

CHAPTER IV
NUMERICS

§8. Discretization

To perform numeric simulations of dipole-mediated domains, we discretized the boundary $\partial\Omega$ in the energy expression (5.2). Consider a set of N points $\vec{x}_i = (x_i, y_i)$, each equidistant from its adjacent neighbors. Note that we will treat the \vec{x}_i as indexed periodically, so that $\vec{x}_{N+i} = \vec{x}_i$. The condition of equidistance can be expressed by the set of N consistency equations

$$\frac{L}{N} = \|\vec{x}_{i+1} - \vec{x}_i\| \quad (8.1)$$

Define $\vec{\rho}_i \equiv \frac{1}{2}(\vec{x}_{i+1} + \vec{x}_i)$ and $\vec{t}_i \equiv \frac{1}{2}(\vec{x}_{i+1} - \vec{x}_i)$ to be the position and tangent vectors of boundary points, respectively. It should be easy to see that \vec{t}_i does indeed lie tangent to $\vec{\rho}_i$ for all $i = 1, \dots, N$. We will also denote by \hat{t}_i the unit vector in the \vec{t}_i direction and by \hat{n}_i the unit vector orthogonal to \vec{t}_i and oriented outwards. The obvious discretization of the energy given this discrete system is given by

$$F = \Lambda L - \frac{1}{2} \sum_{i=1}^N \sum_{j=-\frac{N-1}{2}}^{\frac{N-1}{2}} \left(\frac{\hat{t}_{i+j} \cdot \hat{t}_j}{\|\vec{\rho}_{i+j} - \vec{\rho}_j\|} - \frac{1}{\frac{L}{N}|j|} \right) \frac{L^2}{N^2} - L \log L + \sum_{i=1}^N \vec{\Pi}(\vec{x}_i) \cdot \hat{n}_i \frac{L}{N}$$

Here, we have changed the integrals to sums over the boundary points and the measures to the distance between adjacent points, L/N . The only other nontrivial change comes from writing $\sigma \rightarrow jL/N$, which corresponds to the polygonal arc length at the index j . The expression above can be simplified considerably by computing the sum over the second term in the summand and reparameterizing the sum, yielding

$$F = (\Lambda + H_{\frac{N-1}{2}})L - \frac{1}{2} \sum_{i=1}^N \sum_{\substack{j=1 \\ j \neq i}}^N \frac{\vec{t}_i \cdot \vec{t}_j}{\|\vec{\rho}_i - \vec{\rho}_j\|} - L \log L + \sum_{i=1}^N \vec{\Pi}(\vec{x}_i) \cdot \vec{n}_i \quad (8.2)$$

where $\vec{n}_i = \frac{L}{N} \hat{n}_i$ and H_n is the n th harmonic number, defined by

$$H_n = \sum_{k=1}^n \frac{1}{k}$$

The harmonic numbers can also be defined for positive real n by

$$H_n = \gamma + \psi_0(n+1) = \log n + \gamma + \frac{1}{2n} - \frac{1}{12n^2} + \mathcal{O}(n^{-4})$$

where ψ_0 is the digamma function. The area of this polygon approximation is given simply by the sum over the areas of triangles made by the origin and pairs of adjacent points. To ensure that the area of a domain stays constant, this polygon area must fulfill the consistency expression

$$\pi = \frac{1}{2} \sum_{i=1}^N \|\vec{x}_{i+1} \times \vec{x}_i\| = \frac{1}{2} \sum_{i=1}^N (x_i y_{i+1} - x_{i+1} y_i) \quad (8.3)$$

This form of the energy allows us to simulate domains as a set of points representing their boundary. We have now constructed a numeric system involving an energy function (8.2) under the explicit constraints (8.1) and (8.3). Our principle interest will be to minimize that energy without violating the constraints. Before we describe the methods and algorithms involved in performing this constrained minimization, we will introduce two forms for $\bar{\Pi}$, the external line potential.

§9. Random Background

In §16, we will want to simulate the effect of an inhomogeneous substrate on fluid domains. To do this, we implement a static random energy background that we can then relax domains atop. The form of the random energy background will be a superposition of random plane waves. The set of waves is constructed in the following way. First, we choose positive real numbers k_0 and a_0 to characterize the scale of the noise and an integer M to give the number of modes included. Then, we create a set of vectors $\{\vec{k}_i\}$ and sets of scalars $\{a_i\}$ and $\{\phi_i\}$, where $i = 1, \dots, M$. The \vec{k}_i are taken from a uniform distribution in the circle of radius k_0 centered at the origin, the a_i are taken uniformly from the interval $[0, 2a_0/M]$, and the ϕ_i are taken uniformly from the interval $[0, 2\pi]$. The background energy is then given by the density

$$u(\vec{\rho}) = \sum_{i=1}^M a_i \cos(\vec{k}_i \cdot \vec{\rho} + \phi_i)$$

Our choices for the sets $\{\vec{k}_i\}$, $\{a_i\}$ and $\{\phi_i\}$ should be clear now. The background energy is a sum of random sinusoids whose wavenumber is bounded

above by k_0 , and whose average magnitude is

$$\langle |u(\vec{\varrho})| \rangle = \left\langle \left| \sum_{i=1}^M a_i \cos(\vec{k}_i \cdot \vec{\varrho} + \phi_i) \right| \right\rangle = M \langle a_i \rangle_i \langle |\cos x| \rangle = \frac{a_0}{2}$$

whence a_0 gives the mean amplitude of the noise. Consider now the function $\bar{\Pi} : \mathbb{R}^2 \rightarrow \mathbb{R}^2$ defined by

$$\bar{\Pi}(\vec{\varrho}) = \frac{1}{2} \sum_{i=1}^M a_i \sin(\vec{k}_i \cdot \vec{\varrho} + \phi_i) \begin{bmatrix} k_{ix}^{-1} \\ k_{iy}^{-1} \end{bmatrix}$$

It follows that

$$\vec{\nabla} \cdot \bar{\Pi} = \frac{\partial \Pi_x}{\partial x} + \frac{\partial \Pi_y}{\partial y} = \sum_{i=1}^M a_i \cos(\vec{k}_i \cdot \vec{R} + \phi_i) = u$$

This is precisely the condition we have on the external line potential $\bar{\Pi}$ from §4. Therefore, the energy due to this potential is given from (4.1) by

$$\begin{aligned} F_{\text{rand}} &= \oint_{\partial\Omega} \bar{\Pi} \cdot \hat{n} \, ds = \oint_{\partial\Omega} (\Pi_x \hat{n}_x + \Pi_y \hat{n}_y) \, ds \\ &= \frac{1}{2} \oint_{\partial\Omega} \sum_{i=1}^M a_i \sin(\vec{k}_i \cdot \vec{R} + \phi_i) \left(\frac{\hat{t}_y}{k_{ix}} - \frac{\hat{t}_x}{k_{iy}} \right) \, ds \end{aligned}$$

where we have used $\hat{n}_x = \hat{t}_y$ and $\hat{n}_y = -\hat{t}_x$, true for the tangents and normals of positively oriented domains. This means that, given the discretization of the domain boundary we used in the previous section,

$$F_{\text{rand}} = \frac{1}{2} \sum_{j=1}^N \sum_{i=1}^M a_i \sin(\vec{k}_i \cdot \vec{R}_j + \phi_i) \left(\frac{y_{j+1} - y_j}{k_{ix}} - \frac{x_{j+1} - x_j}{k_{iy}} \right) \quad (9.1)$$

where the first sum is over the points making up the sides of the domain and the indices are defined cyclically. We can now simulate domains over such backgrounds by simply adding this term to the energy (8.2).

§10. Confining Well

We may also want to confine our domains to a finite region of the plane. However, we cannot use our boundary energy method without a potential that is everywhere smooth, so that Green's theorem can operate as normal. Therefore, we want to use an energy density that is nearly zero for most of the confining region and goes quickly to a value much larger than the standard domain energy at the edge of that region. For a square region of size $2w$, we can write

$$u_{\text{well}}(\vec{\varrho}) = e^{s(x-w)} + e^{-s(x+w)} + e^{s(y-w)} + e^{-s(y+w)}$$

where s gives an idea of the steepness of the well. In this case, the total energy of the well would be

$$\begin{aligned} F_{\text{well}} &= \iint_{\Omega} u_{\text{well}} \, dA \\ &= \iint_{\Omega} \left(e^{s(x-w)} + e^{-s(x+w)} + e^{s(y-w)} + e^{-s(y+w)} \right) \, dA \end{aligned}$$

We would like to use Stokes theorem to convert this to a line integral. Consider the function $\vec{\Pi} : \mathbb{R}^2 \rightarrow \mathbb{R}^2$ defined by

$$\vec{\Pi}(\vec{x}) = \frac{1}{s} \begin{bmatrix} e^{s(x-w)} - e^{-s(x+w)} \\ e^{s(y-w)} - e^{-s(y+w)} \end{bmatrix}$$

It follows that

$$\vec{\nabla} \cdot \vec{\Pi} = \frac{\partial \Pi_x}{\partial x} + \frac{\partial \Pi_y}{\partial y} = e^{s(x-w)} + e^{-s(x+w)} + e^{s(y-w)} + e^{-s(y+w)} = u_{\text{well}}$$

Therefore, by Stokes theorem,

$$\begin{aligned} F_{\text{well}} &= \iint_{\Omega} \vec{\nabla} \cdot \vec{\Pi} \, dA = \oint_{\partial\Omega} \vec{\Pi} \cdot \hat{n} \, ds = \oint_{\partial\Omega} (\Pi_x \hat{n}_x + \Pi_y \hat{n}_y) \, ds \\ &= \frac{1}{s} \oint_{\partial\Omega} \left[\left(e^{s(x-w)} - e^{-s(x+w)} \right) \hat{t}_y - \left(e^{s(y-w)} - e^{-s(y+w)} \right) \hat{t}_x \right] \, ds \end{aligned}$$

where we have used $\hat{n}_x = \hat{t}_y$ and $\hat{n}_y = -\hat{t}_x$, true for the tangents and normals of positively oriented domains. This means that, given the discretization of the domain boundary we are using,

$$\begin{aligned} F_{\text{well}} &= \frac{1}{s} \sum_{j=1}^N \left[\left(e^{s(x_j-w)} - e^{-s(x_j+w)} \right) (y_{j+1} - y_j) - \right. \\ &\quad \left. - \left(e^{s(y_j-w)} - e^{-s(y_j+w)} \right) (x_{j+1} - x_j) \right] \end{aligned} \quad (10.1)$$

This expression provides the desired energy well by simply adding this energy term to the energy in (8.2).

§11. Lagrange's Method

We now have a constrained numeric system for which we would like to find the minimizers of an energy function. Therefore, we will turn to the method of Lagrange multipliers. It is well known from elementary calculus that an optimization problem in N variables of the function f under the M constraints

$g_i = 0$ ($i = 1, \dots, M$) is equivalent to the unconstrained optimization problem in $N + M$ variables of the new function

$$\mathcal{L} \equiv f - \sum_{i=1}^M \lambda_i g_i$$

The function \mathcal{L} is known as the *Lagrangian* of the system, and the new system variables λ_i , $i = 1, \dots, M$, are known as *Lagrange multipliers*. When \mathcal{L} is minimized, it is clear that f is minimized *and* the constraints are satisfied, since minimization of \mathcal{L} implies that $\vec{\nabla} \mathcal{L} = 0$ and that

$$0 = \frac{\partial \mathcal{L}}{\partial \lambda_i} = -g_i$$

for all $i = 1, \dots, M$. However, the converse is not, in general, true. That is, if x is a critical point of f which satisfies the constraints and minimizes f , then while there exists an extension of x to \mathbb{R}^{N+M} such that that extension is a critical point of \mathcal{L} which satisfies the constraints, it does not necessarily minimize \mathcal{L} . The reason for this is that the Lagrange multipliers may be metastable at this point, though these parameters do not actually affect the stability of the system being modelled.

This fact becomes important when we want to do stability analysis of any numeric result using a Lagrange multiplier system. Normally, if

$$Hf \equiv \begin{bmatrix} \frac{\partial^2 f}{\partial x_1^2} & \frac{\partial^2 f}{\partial x_1 \partial x_2} & \cdots & \frac{\partial^2 f}{\partial x_1 \partial x_N} \\ \frac{\partial^2 f}{\partial x_2 \partial x_1} & \frac{\partial^2 f}{\partial x_2^2} & \cdots & \frac{\partial^2 f}{\partial x_2 \partial x_N} \\ \vdots & \vdots & \ddots & \vdots \\ \frac{\partial^2 f}{\partial x_N \partial x_1} & \frac{\partial^2 f}{\partial x_N \partial x_2} & \cdots & \frac{\partial^2 f}{\partial x_N^2} \end{bmatrix}$$

is the Hessian matrix of the function $f(x_1, \dots, x_N)$, the function f is at a minimum (or the system it describes is stable) if the eigenvalues of Hf are positive. However, this is no longer true of a system described by a Lagrangian. Rather, such a system is stable if the *generalized eigenvalues* μ of the Hessian for the Lagrangian that describes that system are all positive. μ is a generalized eigenvalue of a Lagrangian $\mathcal{L}(x_1, \dots, x_N, \lambda_1, \dots, \lambda_M)$ if there exists a vector $\vec{v} \in \mathbb{R}^{N+M}$ such that

$$(H\mathcal{L})\vec{v} = \mu \begin{bmatrix} I_N & 0 \\ 0 & 0 \end{bmatrix} \vec{v} \quad (11.1)$$

where I_N is the $N \times N$ identity matrix and

$$H\mathcal{L} \equiv \begin{bmatrix} \frac{\partial^2 \mathcal{L}}{\partial x_1^2} & \cdots & \frac{\partial^2 \mathcal{L}}{\partial x_1 \partial x_N} & \frac{\partial^2 \mathcal{L}}{\partial x_1 \partial \lambda_1} & \cdots & \frac{\partial^2 \mathcal{L}}{\partial x_1 \partial \lambda_M} \\ \vdots & \ddots & \vdots & \vdots & \ddots & \vdots \\ \frac{\partial^2 \mathcal{L}}{\partial x_N \partial x_1} & \cdots & \frac{\partial^2 \mathcal{L}}{\partial x_N^2} & \frac{\partial^2 \mathcal{L}}{\partial x_N \partial \lambda_1} & \cdots & \frac{\partial^2 \mathcal{L}}{\partial x_N \partial \lambda_M} \\ \frac{\partial^2 \mathcal{L}}{\partial \lambda_1 \partial x_1} & \cdots & \frac{\partial^2 \mathcal{L}}{\partial \lambda_1 \partial x_N} & 0 & \cdots & 0 \\ \vdots & \ddots & \vdots & \vdots & \ddots & \vdots \\ \frac{\partial^2 \mathcal{L}}{\partial \lambda_M \partial x_1} & \cdots & \frac{\partial^2 \mathcal{L}}{\partial \lambda_M \partial x_N} & 0 & \cdots & 0 \end{bmatrix}$$

is the Hessian matrix extended to the multiplier variables. This new stability condition will also be important when we begin to discuss the algorithms we choose to use. An algorithm that strictly minimizes the Lagrangian is disadvantageous because it necessarily ignores solutions for which the multipliers are at saddle points. In fact, it is not hard to see that a minimization routine will nearly always diverge on a multiplier system, since the multipliers themselves are not bounded from below.

For our system, the Lagrangian is given by the difference between the energy (8.2) and the constraints (8.1) and (8.3), or

$$\mathcal{L} = F - \sum_{i=1}^N \lambda_i \left(\frac{L^2}{N^2} - \|\vec{x}_{i+1} - \vec{x}_i\|^2 \right) - \lambda_A \left(\pi - \frac{1}{2} \sum_{i=1}^N (x_i y_{i+1} - x_{i+1} y_i) \right) \quad (11.2)$$

If we choose to minimize over a random background or in a confining well (or both!), F is simply the energy (8.2) with (9.1) or (10.1) added. This is a numeric system of $2N + 1$ physical variables: x_i and y_i for $i = 1, \dots, N$, and L . In addition, it has $N + 1$ multiplier variables. The state of this system can be described by a state vector $\vec{z} \in \mathbb{R}^{3N+2}$, which looks schematically like

$$\vec{z} = \begin{bmatrix} \vec{x} \\ \vec{y} \\ L \\ \vec{\lambda} \end{bmatrix}$$

This will be the system we consider when there is some nontrivial background potential to break natural symmetries. However, lacking such a potential, we will often make use of a slightly modified system. First, in order to anchor the domain's orientation, we fix the point $y_1 = 0$, reducing the physical variables of the problem to $2N$. Next, we introduce two more constraints to the system: that the 'center of mass' of the boundary points lies at the origin, or

$$0 = \sum_{i=1}^N x_i = \sum_{i=1}^N y_i$$

This also introduces two new Lagrange multipliers to the system, which will be denoted λ_x and λ_y , and raises the number of constraints (and multipliers)

to $N + 3$. The schematic representation of the state vector \vec{z} is the same, albeit with a slightly shorter vector \vec{y} , and now as a vector in \mathbb{R}^{3N+3} .

§12. Algorithms

We now have an explicit unconstrained numeric system with which to work. For the duration of this section, we will denote the number of physical variables as N , the number of constraints (and hence multipliers) as M , the state vector of the system by \vec{z} , the non-multiplier variables as x_i , $i = 1, \dots, N$, and the multipliers by λ_i , $i = 1, \dots, M$. While this is inconsistent with the notation of the previous section, it will simplify the discussion of the numerics that follows.

For cases in which we are not concerned with producing stable domains or have some other method of controlling the stability of our results, Newton's method of optimization is ideal. Recall that the i th step of Newton's method is given by

$$\Delta \vec{z}_i = -\alpha [H\mathcal{L}(\vec{z}_i)]^{-1} \vec{\nabla} \mathcal{L}(\vec{z}_i)$$

where α is a relaxation parameter used to improve the convergence of the algorithm. The parameter α can be chosen by any number of means, but we will always use the Armijo rule for determining it [2]. Newton's method is very powerful, as it has quadratic convergence, and will quickly converge to the nearest critical point of the function \mathcal{L} . Therefore, in the proceeding sections involving branch-following as a way to investigate stable and metastable solutions, Newton's method is invaluable and its shortcomings (no differentiation between stable and metastable solutions, poor global convergence) are forgivable.

However, there will come times when we wish to relax domains which are very far from their minima and to ensure that those relaxed domains are, in fact, stable. Here, Newton's method proves useless. However, with a slight modification, its shortcomings can be remedied. The *Levenberg–Marquardt algorithm* (LMA) is a well-known modification to Newton's method that provides global convergence and minimization while not giving up the convergence properties of Newton's method near the solution [2]. This algorithm works by using a modified Hessian matrix H_{LMA} defined by

$$H_{\text{LMA}} \mathcal{L} = H\mathcal{L} + \gamma I_{N+M}$$

where I_n is the $n \times n$ identity matrix and γ is an algorithmically determined constant. The i th LMA step is simply the i th Newton's method step with this Hessian substituted for the usual one. The algorithm begins with relatively large γ , so that $H_{\text{LMA}} \mathcal{L} \sim \gamma I_{N+M}$ and the Newton's method step is very close to the gradient, so the algorithm effectively does gradient following. However, as γ is scaled down, the steps smoothly transition from gradient following to the Newton step, so that as one nears a critical point the improved convergence of the latter can kick in.

However, as mentioned in the previous section, we don't actually want to minimize the Lagrangian of our system: we only want to minimize the Lagrangian with respect to the first N variables and keep the final M multipliers constantly at a critical point (so that the constraints are constantly satisfied). Therefore, we use a modified version of the LMA that instead uses the Hessian

$$H'_{\text{LMA}} \mathcal{L} = H \mathcal{L} + \gamma \begin{bmatrix} I_N & 0 \\ 0 & 0 \end{bmatrix}$$

The parameter γ now only scales gradient following for the N real parameters of the system. When γ is sufficiently large*, the Newton's method step resulting from using this Hessian will always decrease \mathcal{L} given that the constraints are satisfied, and will always drive the constraints toward a critical point. We determine the value of γ in our algorithm using a crude measure of convergence. A constant γ_0 is fixed at the beginning of the algorithm, and after every step the comparison

$$\|\vec{\nabla} \mathcal{L}\| < \frac{\gamma}{\gamma_0}$$

is made. If true, γ is decreased by an order of magnitude. Otherwise, γ is unchanged. For our domains on random backgrounds, γ typically starts at 1 and $\gamma_0 = 1 \times 10^{-7}$. Improvement of the algorithm for determining γ would be a very useful direction for future work on this project.

§13. Implementation

The algorithms described above were implemented in a series of C++ libraries by the author. The code for the core algorithm, our modified LMA, is included in this document in Appendix C. The minimization code, while the core of the numeric system, is only a small piece it. We computed the gradient and Hessian of \mathcal{L} analytically, and produced a large library for creating the gradient and Hessian from a state vector \vec{z} . The exact expressions for the various terms of the gradient can be seen in Appendix B. This appendix is meant to be instructive, and the methods it uses can be easily extended to the calculation of the Hessian as well.

An application was developed for discovering and following bifurcations of domains. This essentially works by slowly varying Λ for a given domain until one of the generalized eigenvalues changes sign, indicating the presence of a critical point. The generalized eigenvector associated with that eigenvalue is then produced and used to perturb the domain at the critical point, pushing it onto the new branch, which can then be traced by continuing to vary Λ . In practice, computing the generalized eigenvalues has a very long runtime compared to making minimization steps, and so eigenvalues are only occasionally computed until a critical point has been found.

*That is, greater than the largest negative generalized eigenvalue of the system's Hessian.

When we begin looking at domains over a random background, we usually begin with a perturbed circular domain and then subject it suddenly to the desired value of Λ , creating large domain structures in one run of the minimization algorithm. Upon minimization, a large collection of *Mathematica* routines were created to plot and otherwise analyze the numeric results. All of the libraries and methods created for this thesis are available at <https://github.com/kentdobias/dipole> under the GPL.

CHAPTER V
 NUMERIC RESULTS

§14. Circle Instabilities & Bifurcations

This section strictly uses the energy expression with an anchored orientation and ‘center of mass’ without an additional potential, as described in the last paragraph of §11. Beginning with a circular domain, we can slowly vary Λ to larger negative values until instabilities of various orders are reached. Each such point is characterized by the change in sign of a generalized eigenvalue of the Hessian of the Lagrangian, as defined in (11.1). In principle, the first such change should happen at Λ_2 , with successive changes occurring at Λ_n for larger integer values of n . We used the first generalized eigenvalue’s sign change to gauge the accuracy of our numeric system. If $\Lambda_2(N)$ is the point that the first generalized eigenvalue of the Hessian for a circular domain becomes zero for a simulated domain on N points, then the error in our numerics for the value of Λ_2 is given by

$$\mathcal{E}(N) = \left| \frac{\Lambda_2 - \Lambda_2(N)}{\Lambda_2} \right|$$

The value of $\mathcal{E}(N)$ for N up to 500 is shown in Fig. 5.1, along with a fit of N^{-2} convergence. As can be seen from that data, our numerics reflect the expected theoretical behavior and converge to it quadratically with the number of points used to model the domain.

At any point on the solution manifold where a generalized eigenvalue of the Hessian becomes zero, there exists a bifurcating solution that branches off from that point in the direction of the corresponding generalized eigenvector. In particular, there is such a solution branching from the circle at every critical Λ_n . The bifurcations corresponding to the circle instabilities will henceforth be referred to as harmonic bifurcations. We developed code which traces solution branches to bifurcating points, then uses the generalized eigenvalue and eigenvector information at the critical point to perturb the state onto the bifurcating solution branch, which can then be traced. Using this methodology, we traced the first five harmonic bifurcations, examples of which can be seen in Fig. 5.2. The branches themselves are represented well by the behavior of their perimeter, L , and the branching in L corresponding to these bifurcations can be seen in Fig. 5.3. That figure also shows the theoretical points at which each of those instabilities occur. As can be seen, the agreement is excellent.

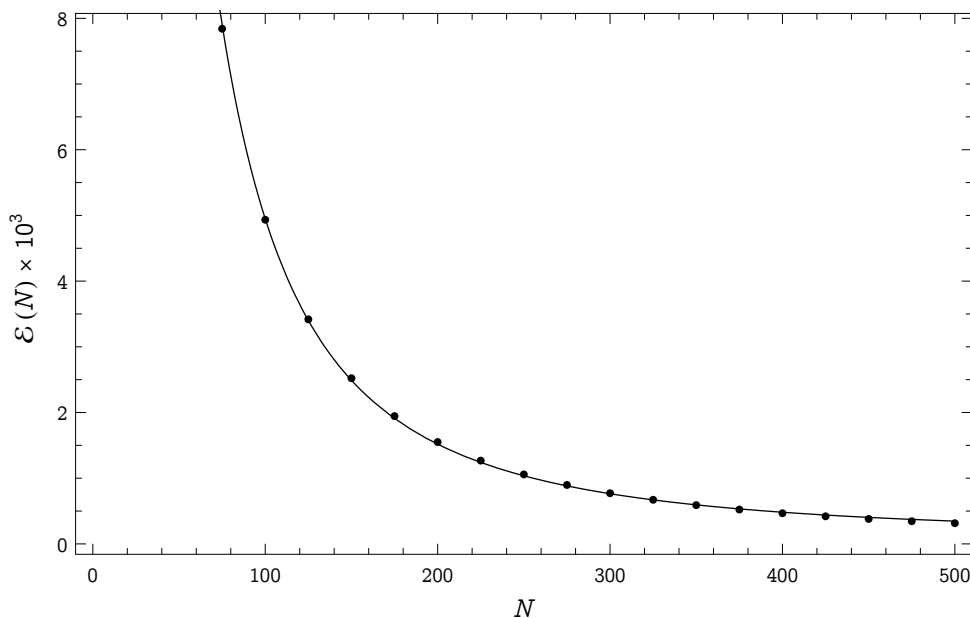


Figure 5.1: The error $\mathcal{E}(N)$ in our numeric approximation of the critical value Λ_2 as a function of the number of boundary points used. The solid line depicts a best fit of N^{-2} .

Fig. 5.3 also shows the stability of these solutions, denoting the stable branches by solid lines and the unstable branches by dotted lines. As can be seen, all of the harmonic bifurcating domains are unstable with the exception of the first, which becomes stable after its subcritical branch. The marked subcritical branches of each bifurcation are also worth noting. This is the first time these branches have been resolved numerically. Examples of the subcritical harmonic bifurcations can be seen in Fig. 5.2(g-1). Theoretical and experimental work Jackson et. al has previously probed the structure of this region of the solution space, but our numerics have fully resolved it [18, 17]. Of particular interest is the bifurcation of the stripe, which in its early evolution is known as the dogbone, from a circular domain. This is the system that was studied by Jackson et. al, and also by McConnell & de Koker [4]. The bifurcation as represented by the perimeter L is shown in Fig. 5.4. The power of this improved resolution is that we can find the value of Λ for the beginning of the upper branch with high precision and accuracy. The branch is found to start at $\Lambda = -1.227$.

In our study of the harmonic bifurcations and their stability, we found several other shapes which bifurcate from these. However, the only stable shapes we found other than the dogbone/stripe were those with threefold junctions, which we call the forked and doubly forked domains. These stable shapes are

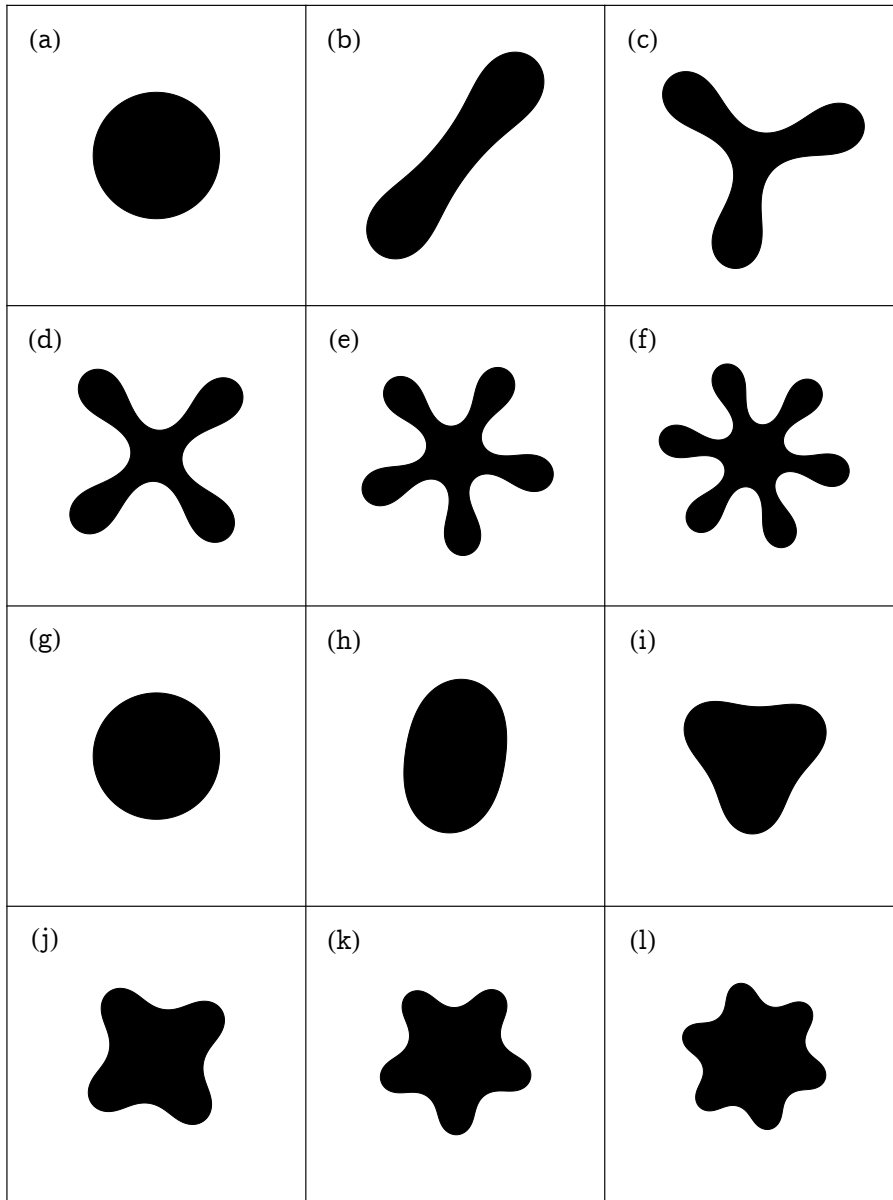


Figure 5.2: A circular domain alongside the first five harmonic bifurcations from a circle. (a-f) Supercritical domain structures. These shapes were taken with Λ values of (a) -1.2 , (b) -1.38 , (c) -1.52 , (d) -1.65 , (e) -1.69 , and (f) -1.77 . (g-l) Subcritical domain structures. These shapes were taken with Λ values of (g) -1.25 , (h) -1.24 , (i) -1.52 , (j) -1.67 , (k) -1.82 , and (l) -2.01 .

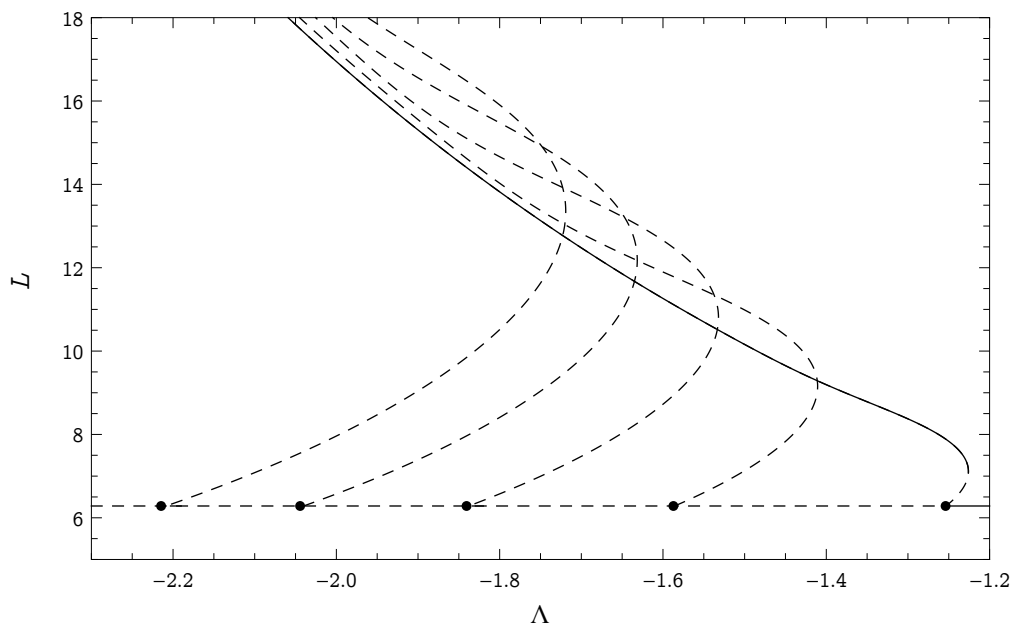


Figure 5.3: The perimeters of the first five harmonic bifurcations from a circular domain. The black dots represent the theoretical bifurcation points Λ_n , the solid lines denote stable numeric solutions, and the dashed lines denote unstable numeric solutions.

shown in Fig. 5.6. The presence of any other higher order junction is associated with the instability of that shape. We also found that, when compared with any stable or metastable shape, the stripe always has a lower energy, lower than even that of the theoretical rectangle. The energies of the harmonic bifurcations along with those of the circle and rectangle are shown in Fig. 5.5. Therefore, we suspect strongly that the stripe domain is the global minimizer after the circle becomes unstable.

§15. Stable Domains

Of particular interest to us are the energy minimizing domain structures. First, it is remarkable that there are so few: the stripe, the forked, and the doubly forked structures. The issue of this scarcity will be resolved in the next section. In the meantime, the study of these stable domains will prove very useful for our eventual analysis of arbitrary domain structures. Representatives of these three domains can be seen in Fig. 5.6.

All three stable morphologies evolve in a similar way, becoming very long and stripe-like with large $-\Lambda$. The perimeter of these domains as a function of Λ can be seen in Fig. 5.7(a). The perimeters of all three evolve exponentially,

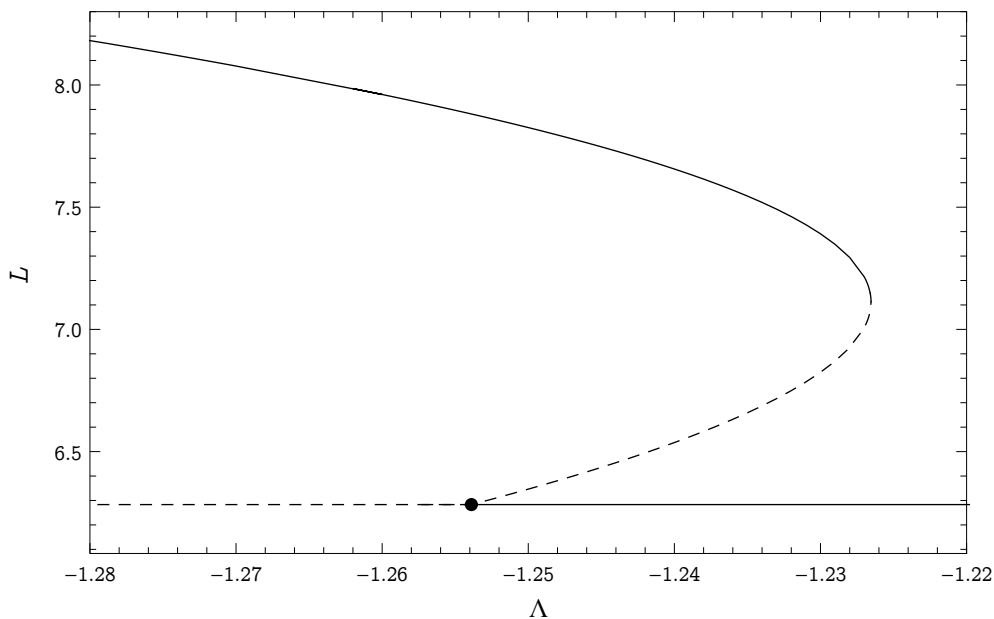


Figure 5.4: The bifurcation of the stripe/dogbone from the circle. The solid lines denote stable numeric solutions and the dashed lines denote unstable ones.

and in fact almost identically to the analytic rectangle perimeter $L_{\text{rec}}(\Lambda)$. The close connection between the perimeters of these stable shapes and that of $L_{\text{rec}}(\Lambda)$ can be seen in Fig. 5.7(b), which shows the relative error between the perimeters of each stable shape and $L_{\text{rec}}(\Lambda)$. As can be seen from that figure, the difference between the perimeters of these shapes and the analytic rectangle becomes less than 2% as quickly as $\Lambda \simeq -2$ and less than 1% at $\Lambda \simeq -2.5$. In fact, even the metastable domains we discovered behave like this, approaching asymptotically the rectangle perimeter as Λ becomes more negative.

Note further that the stripe has a slightly lower perimeter than the rectangle, while the forked and doubly forked domains have progressively higher perimeters. The central bulk of the stripe is geometrically identical to the rectangle in all respects. Therefore, the curved ends of the stripe domain must be responsible for the deviation. These ends have a size proportional to the width of the stripe, which is in turn proportional to $w_{\text{rec}}(\Lambda)$, the asymptotic rectangle width. The difference between the perimeters of the stripe domain and the rectangle should likewise be proportional to the size of the anomalous ends. Hence, in the limit of large negative Λ , the expressions

$$\frac{L_{\text{stripe}} - L_{\text{rec}}}{w_{\text{rec}}} \qquad \frac{L_{\text{double}} - 2L_{\text{forked}} - L_{\text{rec}}}{w_{\text{rec}}} \qquad (15.1)$$

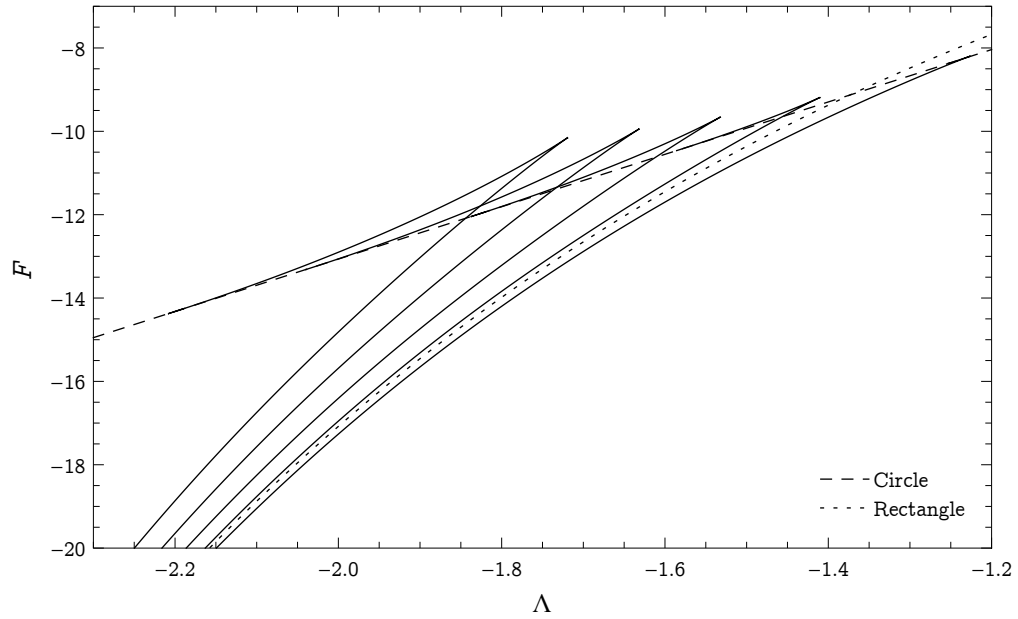


Figure 5.5: The energies of the first five harmonic bifurcations from a circular domain. The solid lines denote those numeric solutions, the dashed line denotes the theoretic circle energy, and the dash-dotted line denotes the theoretic rectangle energy.

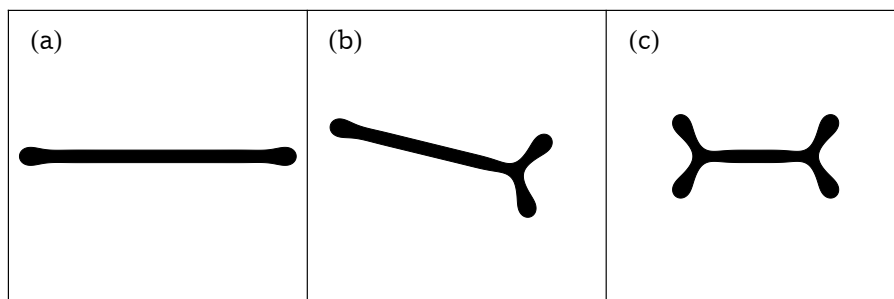


Figure 5.6: Representatives of (a) stripe, (b) forked, and (c) doubly forked domain morphologies at $\Lambda = -2$. These are the only stable morphologies in the absence of a random energy backdrop.

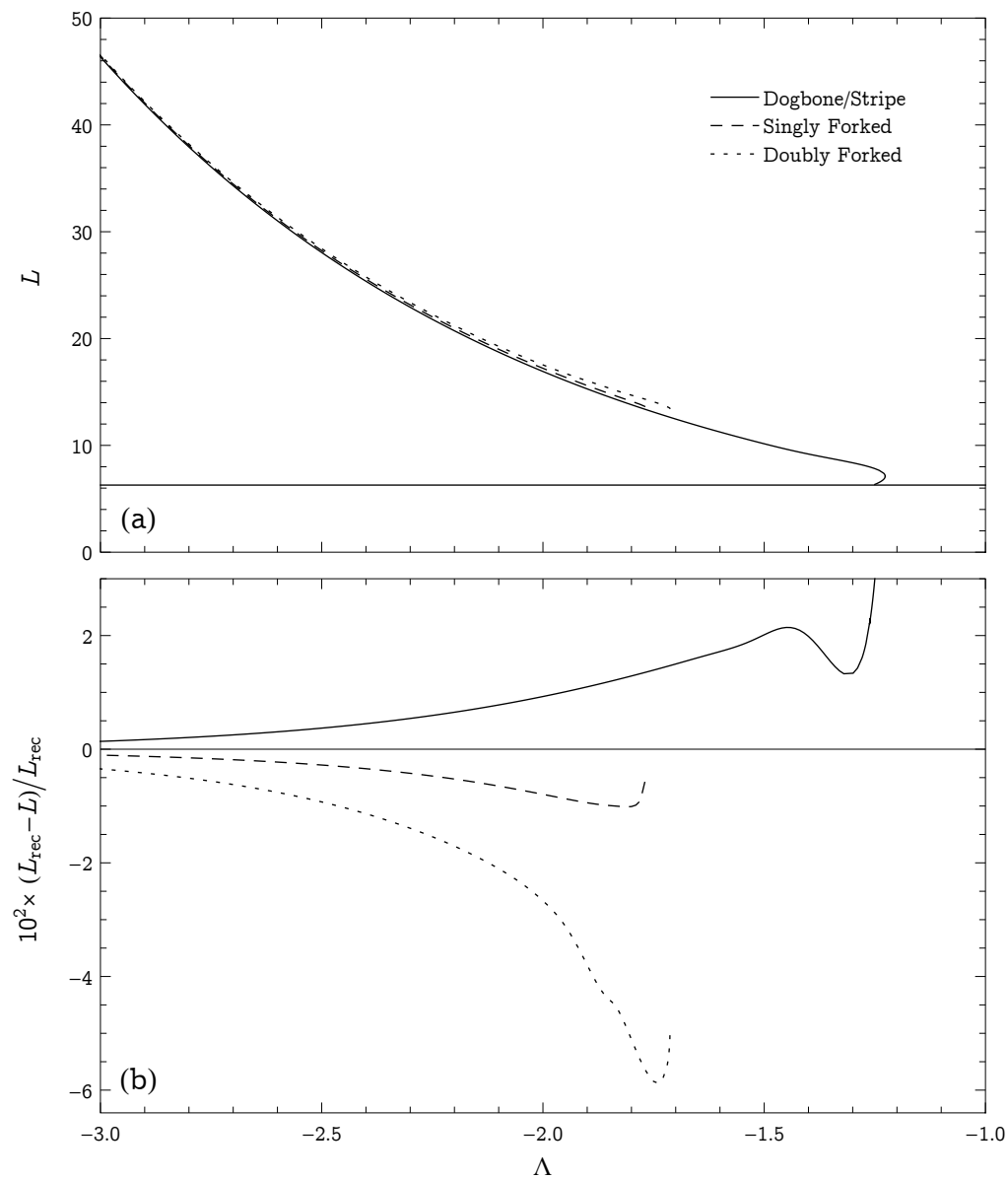


Figure 5.7: The asymptotic behavior of the perimeter of the three stable domain morphologies for $N = 8196$. (a) The perimeter of each morphology as a function of Λ . (b) The relative error between the perimeter of each morphology and L_{rec} , the asymptotic rectangle perimeter.

should go to the same constant c . This is a nontrivial statement, since w_{rec} decreases exponentially as Λ becomes more negative, so $L_{\text{stripe}} - L_{\text{rec}}$ will have to decrease equally exponentially in order for c to converge. However, this is exactly what we see. Both expressions in (15.1) can be seen plotted as a function of Λ in Fig. 5.8(a–b) for various N . As can be seen in that figure, resolving the constant c pushed our numerics to their limit because of the fine nature of the differences involved. Also plotted is a line denoting the *Richardson extrapolation* calculated from the $N = 4096$ and $N = 8192$ curves. Richardson extrapolation is a way to improve the accuracy of a numeric model by extrapolating its behavior at various N . Though our numerics have appreciable error, especially as Λ approaches -3 or so, the constant convergence is evidenced clearly nonetheless. The constant itself can be roughly determined by sampling along the relatively constant region between -2.8 and -3.1 and averaging, yielding $c = -0.482 \pm 0.001$.

In addition, we need to account for the perimeter differences of the forked and doubly forked domains. When a threefold junction is added to a stripe-like shape, another anomalous end is added. Like the ends, the size of the junction itself also scales with the width of the domain. Therefore, we should expect that there is a *cost per threefold junction* which scales like $w_{\text{rec}}(\Lambda)$, so that in the limit of large negative Λ , the expressions

$$\frac{L_{\text{forked}} - L_{\text{stripe}}}{w_{\text{rec}}} \quad \frac{L_{\text{double}} - L_{\text{forked}}}{w_{\text{rec}}} \quad \frac{L_{\text{double}} - L_{\text{stripe}}}{2w_{\text{rec}}}$$

should go to the same constant m . As can be seen in Fig. 5.8(c–e), this is indeed the case. All three ratios tend to the same constant, which can be determined to be $m = 0.819 \pm 0.001$ by averaging the Richardson extrapolation for each at a variety of sample points. For both constants m and c , the errors are given by standard deviations of the sample set.

Given this description, one might imagine that the perimeter of any simply connected domain with n threefold junctions and no junctions of higher order will be, for sufficiently high Λ ,

$$L = L_{\text{rec}} + (c + mn)w_{\text{rec}}$$

This is a remarkably simple characterization of complicated domain structure, but, as we will see, it indeed holds for domains which resemble the intricate structure of those seen in experiment. Though this model necessarily restricts itself to domains with threefold junctions, recall that we only found stable shapes with threefold junctions. As it turns out, junctions of higher order are never seen in stable shapes in our forthcoming numerics, and rarely seen in experimental domains. Therefore, this model is almost entirely general.

§16. Domains Over Random Backgrounds

Finally, we return to the question which should have been gnawing at the reader throughout the previous two sections: why do the stable (and even

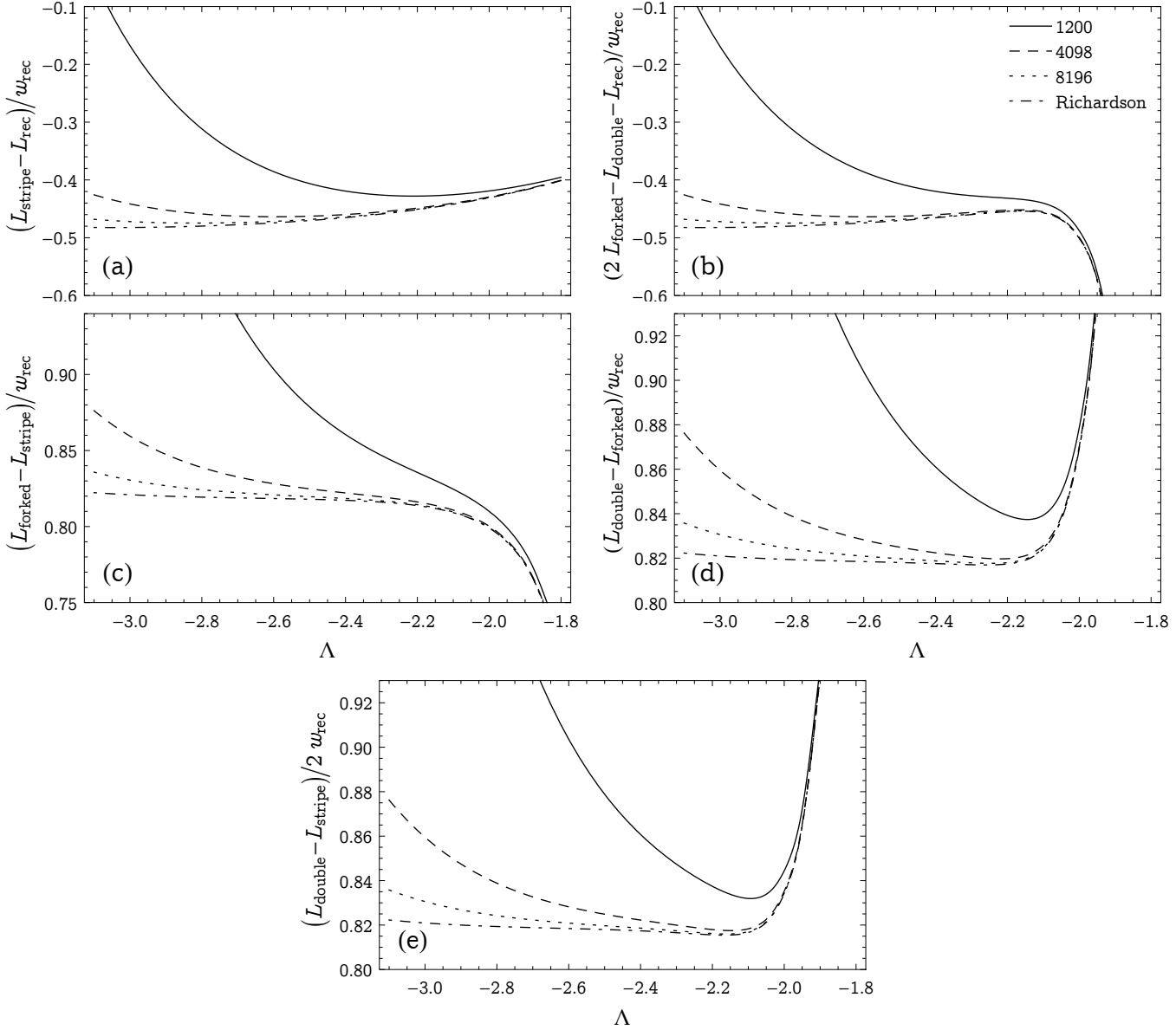


Figure 5.8: The ratios of the rectangle width w_{rec} to linear combinations of the perimeters of the (a) stripe and rectangle, (b) doubly forked, forked, and rectangle, (c) forked and stripe, (d) doubly forked and forked, and (e) doubly forked and stripe domains. Each is plotted at $N = 1200, 4096, 8192$, and the Richardson extrapolation between 4096 and 8192.

metastable) domain morphologies resemble so little of the richness seen in experimental settings? This is because the domains considered in the previous two sections were generated in a distinctly unexperimental setting: over zero background potential $u(r)$. In reality, no film or confined fluid rests on a perfectly homogeneous and passive substrate, but instead must contend with both microscopic interactions with the substrate material and possibly domain-scale inhomogeneities in the material surface. This will inevitably cause a coarsening in the energy landscape of the fluid: adjacent points on the substrate may contribute slightly differently to the energy of the domain resting over them.

Imagine two branches of the branching structure typical of dipole-mediated systems, like those in Fig. 5.9. Our analysis of the threefold harmonic shape suggests such a configuration is unstable and will decay by shortening one branch down into the other. We wish to find the energy gradient associated with this decay. Consider a small cross section of the upper branch. We will roughly compute the energy it takes to move this piece onto the lower branch. Since such a move conserves the perimeter of the shape, the line tension and logarithmic terms in the energy do not change. The dipole energy of the small section with respect to the bulk scales like the area of the section, $w_{\text{rec}} \cdot \Delta x$, over the cube of the mean distance of that section from the rest of material, which we expect to scale like L_{rec} . There is a scaling constant c_1 that depends on the geometry of the bulk relative to the upper branch. Upon moving to the lower branch, the scaling behavior is identical, but the bulk relation constant changes to c_2 . Therefore, we have

$$\Delta F = \frac{w_{\text{rec}} \Delta x}{L_{\text{rec}}^3} (c_2 - c_1)$$

Using the known scaling behavior of L_{rec} and w_{rec} , this can be written

$$\frac{\Delta F}{\Delta x} \sim e^{4(\Lambda+1)}$$

Thus, as Λ becomes negative, like it does in the regime where we see branching structures emerge, the energy gradient which destroys branching structures becomes smaller exponentially. Therefore, as Λ gets to around -2 , we should expect to see branching structures begin to emerge over random backgrounds of even modest amplitude, say, $a_0 \sim 10^{-4}$.

We now anneal domains on the random background described in §9. Recall that our strategy for creating domains with complex branching structure was to begin with a perturbed circular domain sitting atop the random background, then immediately minimize this at some high Λ value. An example of the resulting domain morphologies can be seen in Fig. 5.10. As that figure shows, branching structures do emerge quickly as Λ becomes more negative. The domain morphologies pictured here are only a limited selection of the ones we were able to generate, and both these and the others resemble experimental domains qualitatively.

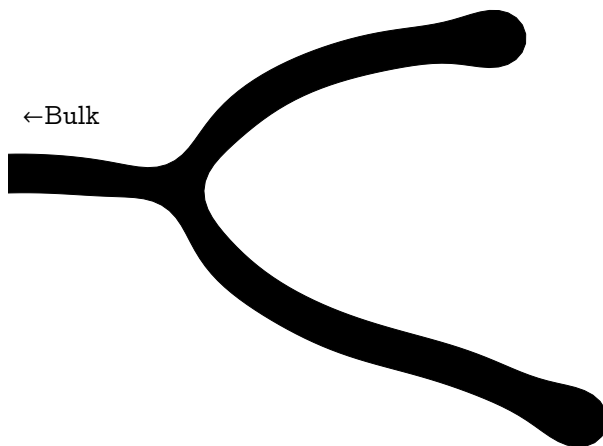


Figure 5.9: An example of two branches in a more complex branching domain.

Domains generated over random backgrounds continue to have perimeters which closely resemble the asymptotic rectangle perimeter L_{rec} . Fig. 5.11(a) shows the perimeters of a collection of such domains plotted with L_{rec} , and Fig. 5.11(b) shows the relative error of those perimeters from the rectangle perimeter. As can be seen, the asymptotic rectangle perimeter describes the perimeters of far more complex shapes up to about 5%. The description begins to get worse, however, with large Λ . This is due to the steady increase in the number of threefold junctions seen in shapes as a function of Λ . This increase is detailed in Fig. 5.12. As we saw previously, increasing the number of threefold junctions causes the perimeter to get larger than the rectangle approximation predicts, and this is precisely what we observe in our random domains.

Recall our model for the perimeter of a domain; that is, if a domain has n threefold junctions, then

$$L = L_{\text{rec}} + (c + mn)w_{\text{rec}}$$

where c and m were constants computed earlier using our data for the stable shapes. We can use this empirical rule to solve for Λ in terms of L and n , yielding

$$\Lambda' = \log \left[\frac{L - \sqrt{L^2 - 8\pi(c + mn)}}{2(c + mn)} \right] - 1 \quad (16.1)$$

Here Λ' is used to denote values of Λ that our rule predicts as opposed to those that were used to generate the domain (the ‘true’ value of Λ). Since c and m have an error associated with them, Λ' also does, and this is given by

$$\delta\Lambda' = \frac{4\sqrt{2}\pi(c + mn)\sqrt{\delta c^2 + n \delta m^2}}{\sqrt{L^2 - 8\pi(c + mn)} - [L^2 - 8\pi(c + mn)]}$$

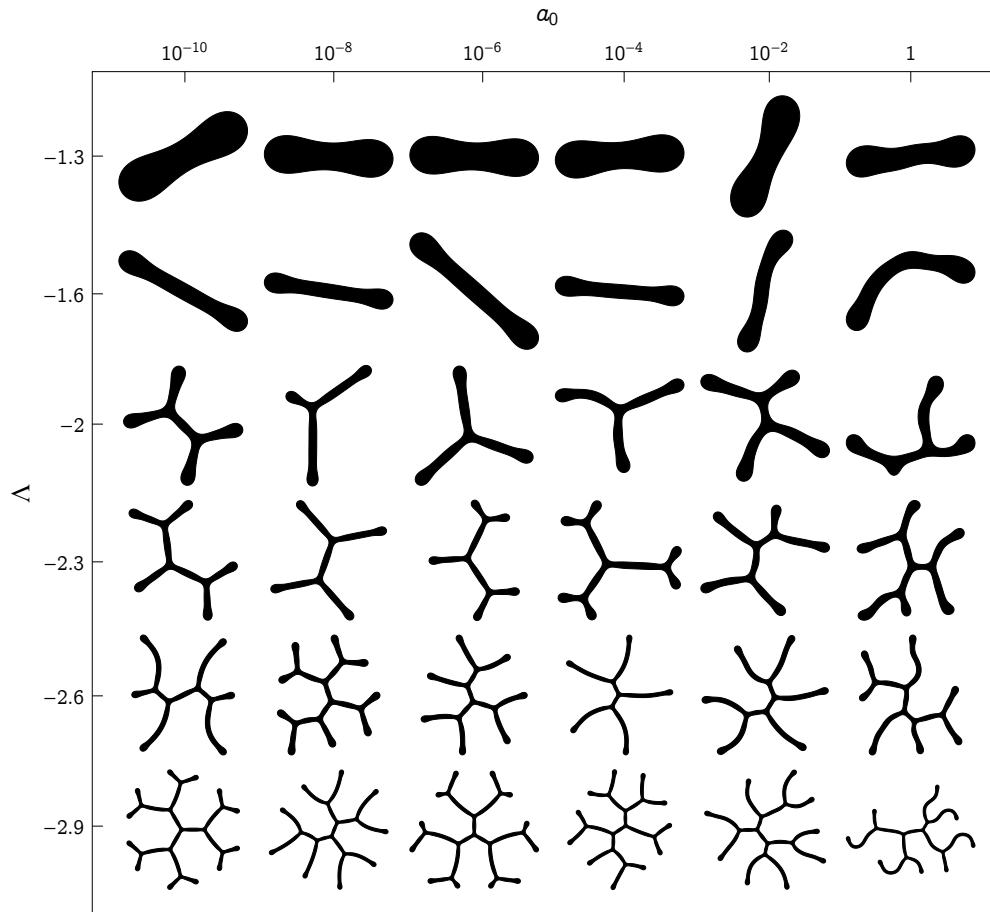


Figure 5.10: A sampling of stable domains generated over a random energy background. Moving along the x axis corresponds to changing a_0 , the average magnitude of the background, and moving along the y axis changes Λ . Note that though all shapes are sized to fit in equally sized boxes, each has the same area in reality. All domains shown here have $N = 1200$.

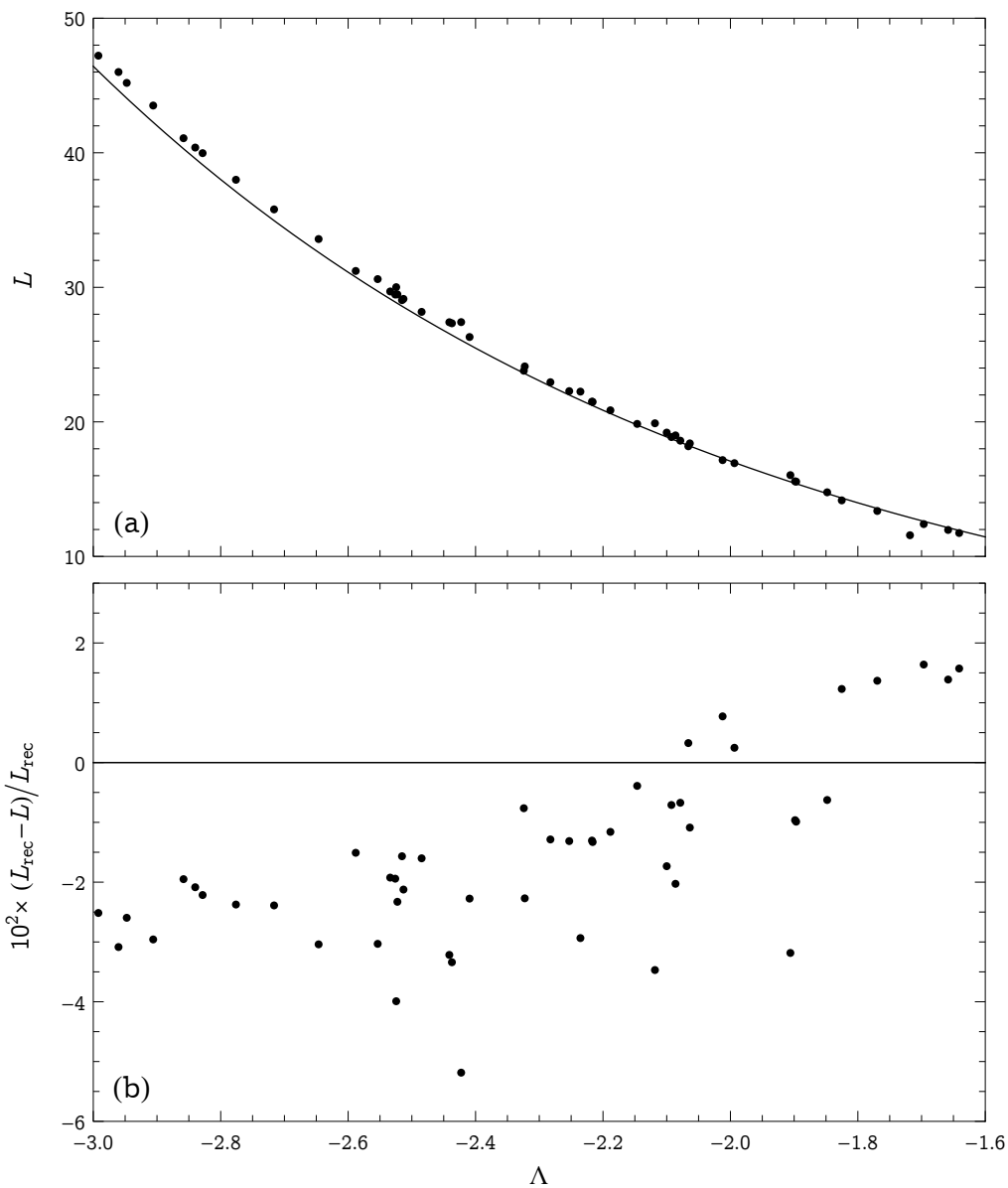


Figure 5.11: (a) The perimeters of domains generated over random energy backgrounds as a function of Λ . The solid line denotes $L_{\text{rec}}(\Lambda)$. (b) The relative error of those perimeters from the rectangle perimeter. All data is taken from shapes with $N = 1200$.

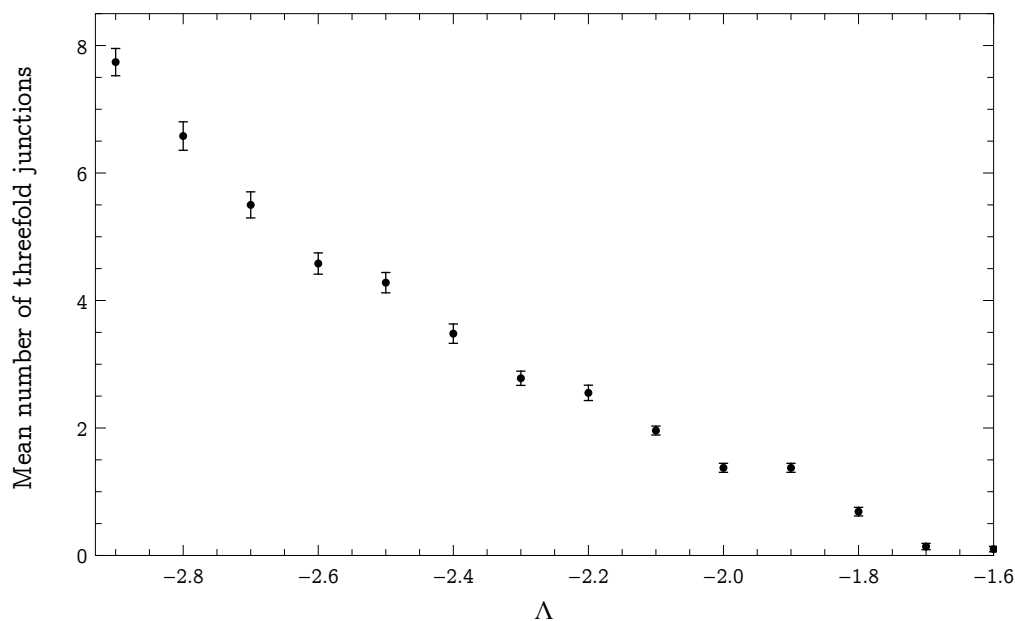
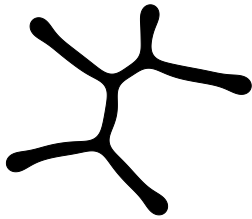
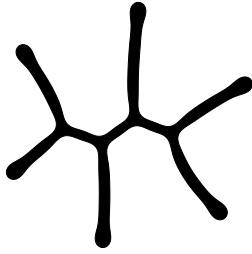
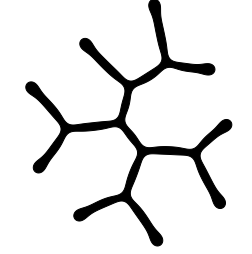
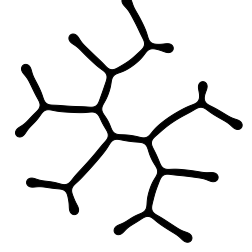


Figure 5.12: The mean number of threefold junctions seen in annealed shapes as a function of Λ . The error bars denote standard error. Data is taken from shapes with $N = 1200$

using standard error propagation. We wish to test the validity of this model on domains generated over a random background. From Fig. 5.8, we clearly must use domains generated on a random background at $N \sim 8192$ if we wish to see accurate results for Λ' , since lower values of N do not result in constant values for c or m . However, the relaxation process at this number of boundary points becomes very computationally taxing, and at the time of this printing we were not able to produce a statistical sample of such domains. We were able to produce a statistical sample of domains at $N = 1200$ points. Despite the clear systematic inaccuracies implied by using data from such domains, the model (16.1) still provides remarkably good agreement with the actual value of Λ the domains were generated at. Four examples of the model analysis are shown in Table 5.1, and Fig. 5.13 shows the mean difference from true Λ for sets of 50 such shapes at a variety of constant Λ . From the figure, the presence of systematic error is clear, and is what we would expect from Fig. 5.8: c and m are effectively larger for domains at $N = 1200$. However, despite the consistent inaccuracies, our simple model is still able to consistently predict Λ' to within 0.5% of Λ in the range $-3 \leq \Lambda \leq -1.6$. Our limited data at $N = 8192$ suggests that this model is indeed valid for domains on random backgrounds *without* systematic error, and is likely to give valid values of Λ for experimental domains. An example of the empirical rule applied to one

Table 5.1: Example domains at $N = 1200$ with generating Λ value, perimeter L , number of threefold junctions n , predicted value Λ' , and prediction error $\delta\Lambda'$.

Shape	Λ	L	n	Λ'	$\delta\Lambda'$
	-2.3	23.519	3	-2.297	0.003
	-2.5	28.853	4	-2.502	0.003
	-2.7	35.445	7	-2.703	0.004
	-2.9	43.386	10	-2.905	0.005

domain at $N = 8192$ can be seen in Table 5.2, and the same analysis done to two experimental domains is shown in Table 5.3. In the case of $N = 8192$, the matching is excellent, and suggests that we may have overestimated the error for c and m . Further numeric work to generate more domains at $N = 8192$ is a clear future direction, as it would allow us to more thoroughly test our model.

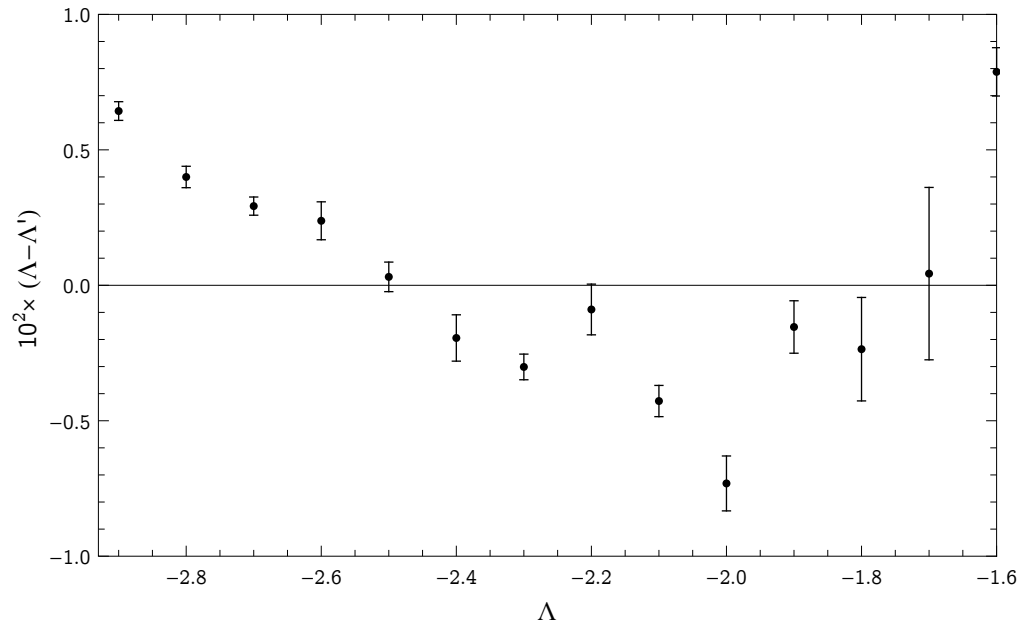


Figure 5.13: The difference between the generating value Λ and the mean predicted value Λ' for domains at $N = 1200$. The error bars denote standard error.

Table 5.2: Example domains at $N = 8192$ with generating Λ value, perimeter L , number of threefold junctions n , predicted value Λ' , and prediction error $\delta\Lambda'$.

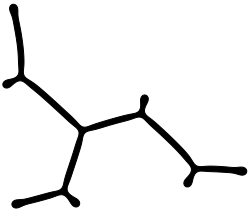

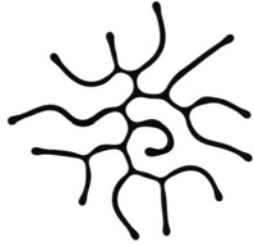
Shape	Λ	L	n	Λ'	$\delta\Lambda'$
	-2.7	35.039	5	-2.6996	0.0035

Table 5.3: Ferrofluids confined to a Hele-Shaw cell, from D. P. Jackson. Table includes dimensionless perimeter L , number of threefold junctions n , predicted value Λ' , and prediction error $\delta\Lambda'$.

Shape	L	n	Λ'	$\delta\Lambda'$
	48.249	7	-3.024	0.004
	56.867	11	-3.185	0.005

§17. Confined Domains

We implemented code to model the confined potential described in §10. Though we have not yet been able to research the role of the packing fraction and the phases of domains within such a confining well, we have been able to confirm that the numerics operate as expected and produce, again, qualitative features seen in experiment. An example of a domain evolving within a confining well can be seen in Fig. 5.14. Two different packing fractions are shown: $f \sim 0.2$ and $f \sim 0.75$. The precise shapes at the ends of the evolution are not entirely trustworthy; at that point, Λ is high enough to exceed our normal accuracy for these domains ($N = 600$). Work on studying confined domains and their morphological phases is an obvious next step in this research.

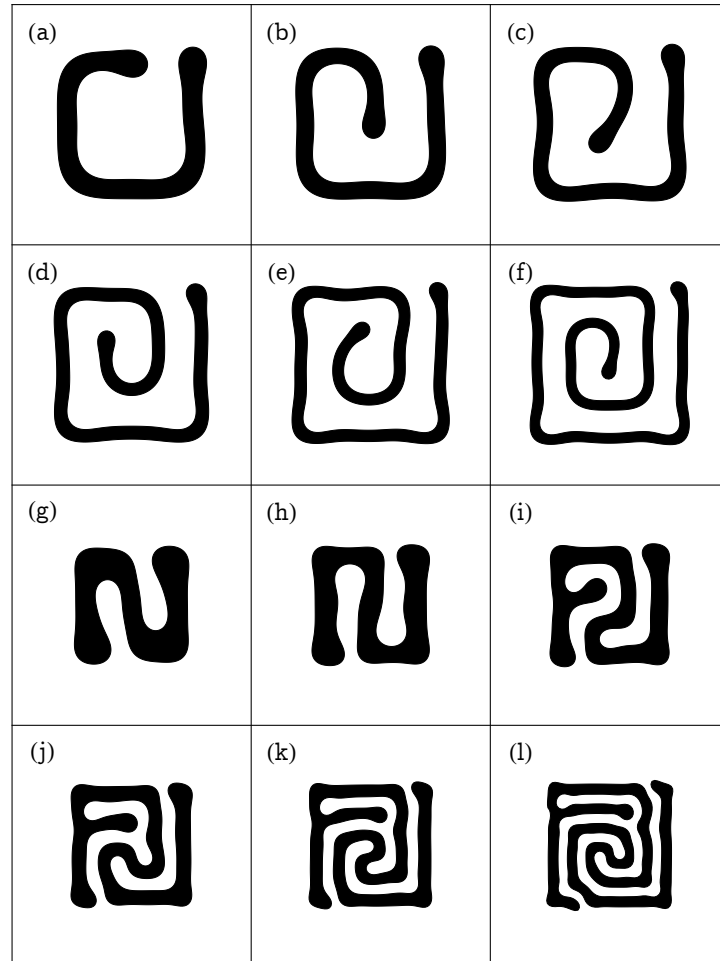


Figure 5.14: Examples of domains in a confining potential. A domain is confined to a square potential and allowed to evolve with slowly varying Λ . (a–f) A domain with packing fraction $f \sim 0.2$. The values of Λ these domains were stable at are (a) -2.11 , (b) -2.25 , (c) -2.39 , (d) -2.53 , (e) -2.67 , and (f) -2.81 . (g–l) A domain with packing fraction $f \sim 0.75$. The values of Λ these domains were stable at are (g) -2.11 , (h) -2.45 , (i) -2.6 , (j) -2.77 , (k) -2.95 , and (l) -3.1 .

CHAPTER VI
CONCLUSIONS

In this thesis, we have developed a new energy formalism for describing dipole-mediated domains and have demonstrated its generality and utility. This formalism is especially powerful in its reduction of the problem to one of a single parameter. This reduction greatly eases our transition to numerics, and allows us to probe the equilibrium morphologies of these shapes to a resolution previously unobtainable.

Using our numeric system, we studied the stability of harmonic bifurcations from the circle and found that most are metastable. Only three asymptotically stable shapes were found: the stripe, singly forked, and doubly forked morphologies. The perimeters of all three of these, as well as that of the metastable results, display the same asymptotic behavior, behavior which is almost identical to that of the simple model of a rectangle which can be calculated exactly and grows exponentially with the negative of the parameter Λ . We developed a consistent description of the perimeters of these shapes in terms of the rectangle perimeter and empirical rules based on the number of threefold junctions present in the shape.

However, the lack of diversity in the resulting stable and metastable domains led us to question where the experimental diversity comes from. We speculated that the discrepancy is due to inhomogeneities present in the substrates of physical domains. The results that come from our simulation of domains on a random energy background indicate strongly that this inhomogeneity is a contributing factor. We also demonstrated that our empirical rule which relates the perimeter and number of threefold junctions in a domain to Λ holds to high accuracy for domains on random backgrounds.

This final result is perhaps our most important. It means that, given just the picture of an experimental domain, we can produce, with both precision and accuracy, the value of Λ . Recall that $\Lambda \equiv \frac{\lambda}{\mu^2} - \log \frac{\Delta}{R}$. Many of the pieces of Λ are easy to determine; R , for instance, only requires knowledge of the area of the domain, and the line tension λ can usually be determined by other means [37]. Therefore, by varying some system parameter like R or μ , one can determine more elusive parameters, like μ or Δ , by fitting to values of Λ at various values of the known parameters. This is effectively a prescription for pulling microscopic information about a complex system out from only information about its equilibrium shape.

This work can be taken in many directions. We only investigated the dynamics of simply connected domains. Allowing other domain genera could be

interesting, and if sufficiently many cuts are made, foaming behavior might be modeled. Also, though we have developed a method for evolving confined domains, we have not taken any time to perform an analysis of their states. Research in how the packing fraction effects the bulk phases of dipole-mediated domains would be very valuable. Finally, our core numerical algorithm uses a rather naïve scaling mechanism for the parameter γ . Developing a more efficient numerical method would be very useful to make more problems tractable using our methods.

HIGHER ORDER ENERGETIC MOMENTS

Consider a two-dimensional fluid where the pair potential between particles is given by r^{-n} for some $n \geq 3$. It follows that the resulting energy contribution of this term is

$$E_n = \frac{\mu_n^2}{2} \iint_{\Omega} \iint_{\Omega} \frac{g(\|\vec{r} - \vec{r}'\|)}{\|\vec{r} - \vec{r}'\|^n} dA' dA$$

In particular, $n = 3$ corresponds to the dipole energy. In order to gauge the contribution of this energy term to an arbitrary domain, we will compute E_n for a domain which covers the upper half-plane. Why is this a useful exercise? If one looks at a fluid domain on a length scale much larger than Δ but much smaller than R , the boundary of the domain will look straight and the opposite boundaries of that domain will look vanishingly far away.

For brevity, we will define

$$u_n(r) \equiv \frac{g(r)}{r^n} \qquad F_n \equiv \frac{E_n}{\mu_n^2}$$

The total energy from this pair potential is then

$$F_n = \frac{1}{2} \iint_{\Omega} \iint_{\Omega} u(\|\vec{r} - \vec{r}'\|) dA' dA$$

Given our assumptions about the form of $g(r)$ in §2, integrating $u(r)$ in a region Δ about some point will result in some finite energetic contribution. We will label this by

$$F_n^0 \equiv \frac{1}{2} \int_0^{2\pi} \int_0^{\Delta} u_n(r) r dr d\theta = \pi \int_0^{\Delta} u_n(r) r dr$$

Note that for $r > \Delta$, $u_n(r) = r^{-n}$, since $g(r) = 1$ in that regime. Parameterizing the energy integral explicitly, we have

$$F_n = \frac{1}{2} \int_0^{\infty} \int_{-\infty}^{\infty} \int_0^{\infty} \int_{-\infty}^{\infty} u_n(\|\vec{r} - \vec{r}'\|) dx' dy' dx dy$$

where

$$\|\vec{r} - \vec{r}'\| = \sqrt{(x - x')^2 + (y - y')^2}$$

We define $x'' \equiv x' - x$ and $y'' \equiv y' - y$. Then, our integral becomes

$$F_n = \frac{1}{2} \int_0^\infty \int_{-\infty}^\infty \int_{0-y}^\infty \int_{-\infty}^\infty u_n(r'') \, dx'' \, dy'' \, dx \, dy$$

where $r'' = \sqrt{x''^2 + y''^2}$. We would now like to convert the inner integrals to polar coordinates. For θ between 0 and π , r'' runs from 0 to ∞ . For θ between π and 2π , r'' is restricted from above by the lower boundary of the domain as $r'' = y \csc \theta$. We therefore have

$$F_n = \frac{1}{2} \int_0^\infty \int_{-\infty}^\infty \left[\int_0^\pi \int_0^\infty u_n(r'') r'' \, dr'' \, d\theta + \int_\pi^{2\pi} \int_0^{y \csc \theta} u_n(r'') r'' \, dr'' \, d\theta \right] dx \, dy$$

The first of these terms is easy to integrate: we have immediately

$$\begin{aligned} F_n &= \frac{1}{2} \int_0^\infty \int_{-\infty}^\infty \left[F_n^0 + \int_0^\pi \int_\Delta (r'')^{-n} r'' \, dr'' \, d\theta + \int_\pi^{2\pi} \int_0^{y \csc \theta} u_n(r'') r'' \, dr'' \, d\theta \right] dx \, dy \\ &= \frac{1}{2} \int_0^\infty \int_{-\infty}^\infty \left[F_n^0 + \frac{\pi \Delta^{-(n-2)}}{n-2} + \int_\pi^{2\pi} \int_0^{y \csc \theta} u_n(r'') r'' \, dr'' \, d\theta \right] dx \, dy \end{aligned} \quad (0.1)$$

In order to simplify our formulae, we define the constant

$$\alpha_n \equiv \frac{1}{2} \left(F_n^0 + \frac{\pi \Delta^{-(n-2)}}{n-2} \right) \quad (0.2)$$

Upon substitution into (0.1), we have

$$F_n = \alpha_n \iint_\Omega dA + \frac{1}{2} \int_\pi^{2\pi} \int_0^{y \csc \theta} u_n(r'') r'' \, dr'' \, d\theta \, dx \, dy$$

If we ascribe our domain with some large but finite area A , then the first integral above can be easily evaluated to yield

$$F_n = \alpha_n A + \frac{1}{2} \int_\pi^{2\pi} \int_0^{y \csc \theta} u_n(r'') r'' \, dr'' \, d\theta \, dx \, dy \quad (0.3)$$

This is simply an energy proportional to the area of the domain, which we assume to be constant. Therefore, it can be safely neglected from the energy expression. We would like to now attack the remaining term in (0.3). For sanity's sake, define

$$\begin{aligned} F_n^1 &\equiv \frac{1}{2} \int_0^\Delta \int_{-\infty}^\infty \int_\pi^{2\pi} \int_0^{y \csc \theta} u_n(r'') r'' \, dr'' \, d\theta \, dx \, dy \\ F_n^2 &\equiv \frac{1}{2} \int_\Delta^\infty \int_{-\infty}^\infty \int_\pi^{2\pi} \int_0^{y \csc \theta} u_n(r'') r'' \, dr'' \, d\theta \, dx \, dy \end{aligned}$$

Clearly, $F_n = F_n^1 + F_n^2$ once the area proportional term is neglected. First, we will consider F_n^1 . Because we lack detailed knowledge of the behavior of $u_n(r)$ for $r < \Delta$, we cannot perform the integral explicitly. However, if we define a function $V_n(y)$ by

$$\frac{\partial V_n}{\partial y} \equiv \int_{\pi}^{2\pi} \int_0^{y \csc \theta} u_n(r'') r'' dr'' d\theta$$

then we may instead write

$$F_n^1 = \frac{1}{2} \int_0^{\Delta} \int_{-\infty}^{\infty} \frac{\partial V_n}{\partial y} dx dy = \frac{1}{2} \int_{-\infty}^{\infty} [V_n(\Delta) - V_n(0)] dx$$

The function $V_n(y)$ should behave sensibly everywhere from 0 to Δ . If we ascribe our domain with some large but finite perimeter l , then we have

$$F_n^1 = \frac{l}{2} [V_n(\Delta) - V_n(0)]$$

Now, we will turn to F_n^2 . Further splitting the limits of integration, we have

$$\begin{aligned} F_n^2 &= \frac{1}{2} \int_{\Delta}^{\infty} \int_{-\infty}^{\infty} \int_{\pi}^{2\pi} \int_0^{y \csc \theta} u_n(r'') r'' dr'' d\theta dx dy \\ &= \frac{1}{2} \int_{\Delta}^{\infty} \int_{-\infty}^{\infty} \left[\int_{\pi}^{2\pi} \int_0^{\Delta} u_n(r'') r'' dr'' d\theta + \int_{\pi}^{2\pi} \int_{\Delta}^{y \csc \theta} u_n(r'') r'' dr'' d\theta \right] dx dy \\ &= \frac{1}{2} \int_{\Delta}^{\infty} \int_{-\infty}^{\infty} \left[F_n^0 + \int_{\pi}^{2\pi} \int_{\Delta}^{y \csc \theta} (r'')^{-n} r'' dr'' d\theta \right] dx dy \\ &= \frac{1}{2} \int_{\Delta}^{\infty} \int_{-\infty}^{\infty} \left[F_n^0 + \int_{\pi}^{2\pi} \left(\frac{\Delta^{-(n-2)}}{n-2} - \frac{(y \csc \theta)^{-(n-2)}}{n-2} \right) d\theta \right] dx dy \\ &= \frac{1}{2} \int_{\Delta}^{\infty} \int_{-\infty}^{\infty} \left[F_n^0 + \frac{\pi \Delta^{-(n-2)}}{n-2} - \frac{\sqrt{\pi} (-y)^{-(n-2)} \Gamma\left(\frac{n-1}{2}\right)}{(n-2) \Gamma\left(\frac{n}{2}\right)} \right] dx dy \end{aligned}$$

Again making use of α_n from (0.2), we have

$$\begin{aligned} F_n^2 &= \frac{1}{2} \int_{\Delta}^{\infty} \int_{-\infty}^{\infty} \left[2\alpha_n - \frac{\sqrt{\pi} (-y)^{-(n-2)} \Gamma\left(\frac{n-1}{2}\right)}{(n-2) \Gamma\left(\frac{n}{2}\right)} \right] dx dy \\ &= \alpha_n A - \alpha_n \Delta \int_{-\infty}^{\infty} dx + \frac{1}{2} \frac{\sqrt{\pi} \Gamma\left(\frac{n-1}{2}\right)}{(n-2) \Gamma\left(\frac{n}{2}\right)} \int_{\Delta}^{\infty} \int_{-\infty}^{\infty} (-y)^{-(n-2)} dx dy \\ &= \alpha_n A - \alpha_n \Delta l + \frac{l}{2} \frac{\sqrt{\pi} \Gamma\left(\frac{n-1}{2}\right)}{(n-2) \Gamma\left(\frac{n}{2}\right)} \int_{\Delta}^{\infty} (-y)^{-(n-2)} dy \end{aligned}$$

Again neglecting the area proportional term, we can now write the total energy,

$$F_n = l \left\{ \frac{1}{2} [V_n(\Delta) - V_n(0)] - \alpha_n \Delta \right\} + \frac{l}{2} \frac{\sqrt{\pi} \Gamma\left(\frac{n-1}{2}\right)}{(n-2) \Gamma\left(\frac{n}{2}\right)} \int_{\Delta}^{\infty} (-y)^{-(n-2)} dy$$

If $n \geq 4$, then we have

$$F_n = l \left\{ \frac{1}{2} [V_n(\Delta) - V_n(0)] - \alpha_n \Delta + \frac{1}{2} \frac{\sqrt{\pi} \Gamma\left(\frac{n-1}{2}\right)}{(n-2)\Gamma\left(\frac{n}{2}\right)} \frac{\Delta^{-(n+3)}}{n-2} \right\}$$

Define the constant λ_n as

$$\lambda_n \equiv \frac{1}{2} [V_n(\Delta) - V_n(0)] - \alpha_n \Delta + \frac{1}{2} \frac{\sqrt{\pi} \Gamma\left(\frac{n-1}{2}\right)}{(n-2)\Gamma\left(\frac{n}{2}\right)} \frac{\Delta^{-(n+3)}}{n-2}$$

Then, we have $F_n = \lambda_n l$. That is, for potentials with $n \geq 4$, the energy contribution is proportional to the perimeter, and the presence of that potential term just adds to the line tension of the domain. However, if $n = 3$ (the dipole term), then we have

$$F_3 = l \left\{ \frac{1}{2} [V_3(\Delta) - V_3(0)] - \alpha_n \Delta \right\} - \frac{l}{2} \frac{\sqrt{\pi} \Gamma\left(\frac{3-1}{2}\right)}{(3-2)\Gamma\left(\frac{3}{2}\right)} \log y \Big|_{y=\Delta}^{y=\infty}$$

Since the logarithm function is unbounded, the final term diverges. In reality, we would evaluate this function at the opposite boundary of the domain, which in this exercise is very far away. What the presence of this divergent term tells us is that we cannot neglect the behavior of the domain's boundary at long distances. This is why the dipole interaction is fundamentally different from the higher order terms: the dipole energy of the resulting domain depends highly on the domain's structure, while the energy contribution from the higher order terms is encapsulated by the line tension in the macroscopic limit.

APPENDIX B

THE GRADIENT OF THE LAGRANGIAN

In this appendix, we show explicitly the calculation of the gradient $\vec{\nabla}\mathcal{L}$ of our numeric system's Lagrangian. Not shown are the calculation for the background and well energies, and that for the Hessian. The analysis here is mostly meant to be instructive, and can be applied identically to the calculation of the Hessian, which follows along identical lines to the gradient but simply has far more terms to consider. If one wishes to see the explicit computation of the Hessian terms, it is done in C++ at <https://github.com/kentdobias/dipole> in the file `domain_energy.cpp`.

Recall that the Lagrangian of our system is given by (11.2) to be

$$\mathcal{L} = F - \sum_{i=1}^N \lambda_i \left(\frac{L^2}{N^2} - \|\vec{x}_{i+1} - \vec{x}_i\|^2 \right) - \lambda_A \left(\pi - \frac{1}{2} \sum_{i=1}^N (x_i y_{i+1} - x_{i+1} y_i) \right)$$

where the energy F is given by (8.2) to be

$$F = (\Lambda + H_{\frac{N-1}{2}})L - \frac{1}{2} \sum_{i=1}^N \sum_{\substack{j=1 \\ j \neq i}}^N \frac{\vec{t}_i \cdot \vec{t}_j}{\|\vec{\ell}_i - \vec{\ell}_j\|} - L \log L$$

In addition, we sometimes impose the additional constraint terms

$$-\lambda_x \sum_{i=1}^N x_i - \lambda_y \sum_{i=1}^N y_i$$

on the Lagrangian, which anchors the center of the domain at the origin. For brevity, we make some redefinitions, writing

$$C_{\text{dist}} \equiv \sum_{i=1}^N \lambda_i \left(\frac{L^2}{N^2} - \|\vec{x}_{i+1} - \vec{x}_i\|^2 \right) \quad C_A \equiv \lambda_A \left(\pi - \frac{1}{2} \sum_{i=1}^N (x_i y_{i+1} - x_{i+1} y_i) \right)$$

$$C_x \equiv \lambda_x \sum_{i=1}^N x_i \quad C_y \equiv \lambda_y \sum_{i=1}^N y_i$$

$$\begin{aligned}
h_{ij} &\equiv \frac{\vec{t}_i \cdot \vec{t}_j}{\|\vec{\ell}_i - \vec{\ell}_j\|} \\
&= \frac{1}{2} \frac{(x_{i+1} - x_i)(x_{j+1} - x_j) + (y_{i+1} - y_i)(y_{j+1} - y_j)}{\sqrt{(x_{i+1} + x_i - x_{j+1} - x_j)^2 + (y_{i+1} + y_i - y_{j+1} - y_j)^2}} \\
F_\mu &\equiv -\frac{1}{2} \sum_{i=1}^N \sum_{\substack{j=1 \\ j \neq i}}^N h_{ij} & F_L &\equiv (\Lambda + H_{\frac{N-1}{2}})L - L \log L
\end{aligned}$$

Using these definitions, we can write the Lagrangian as

$$\mathcal{L} = F - C_{\text{dist}} - C_A - C_x - C_y$$

and the energy as

$$F = F_L + F_\mu$$

By far, the most challenging terms to compute are the derivatives of F_μ , as the double sum in that term provides many possibilities for coordinate combinations. Before we give the derivatives of these energy and Lagrangian components, we first do some preliminary work with the h_{ij} . Notice that h_{ij} is a function of x_i , x_{i+1} , y_i , and y_{i+1} . Since it is symmetric in x_i and y_i , we will only demonstrate the calculations for the x_i derivatives. We will use a derivative index notation for brevity, defining for a function f

$$f_{,i} \equiv \frac{\partial f}{\partial x_i}$$

Define

$$T_{ij} \equiv \vec{t}_i \cdot \vec{t}_j \quad R_{ij} \equiv \frac{1}{4}(x_{i+1} + x_i - x_{j+1} - x_j)^2 + \frac{1}{4}(y_{i+1} + y_i - y_{j+1} - y_j)^2$$

Using this, the summand h_{ij} can be written

$$h_{ij} = T_{ij} R_{ij}^{-1/2}$$

The possible unique nonzero first derivatives of these terms beginning with an i index are

$$\begin{aligned}
T_{ij,i} &= -\frac{1}{4}(x_{j+1} - x_j) & T_{ij,i+1} &= \frac{1}{4}(x_{j+1} - x_j) \\
T_{i(i-1),i} &= \frac{1}{4}(x_{i+1} + x_{i-1} - 2x_i) & R_{ij,i+1} &= \frac{1}{2}(x_{i+1} + x_i - x_{j+1} - x_j) \\
R_{i(i+1),i} &= \frac{1}{2}(x_i - x_{i+2}) & T_{i(i+1),i} &= \frac{1}{4}(x_{i+1} - x_{i+2})
\end{aligned}$$

For $j \neq i, i-1, i+1$, we have

$$\begin{aligned} h_{ij,i} &= T_{ij,i} R_{ij}^{-1/2} + T_{ij}(R_{ij}^{-1/2})_{,i} = T_{ij,i} R_{ij}^{-1/2} - \frac{1}{2} T_{ij} R_{ij}^{-3/2} R_{ij,i} \\ &= -\frac{1}{4} (x_{j+1} - x_j) R_{ij}^{-1/2} - \frac{1}{4} T_{ij} R_{ij}^{-3/2} (x_{i+1} + x_i - x_{j+1} - x_j) \end{aligned}$$

For $j \neq i, i-1$, we have

$$\begin{aligned} h_{(i-1)j,i} &= T_{(i-1)j,i} R_{(i-1)j}^{-1/2} + T_{(i-1)j}(R_{(i-1)j}^{-1/2})_{,i} \\ &= T_{(i-1)j,i} R_{(i-1)j}^{-1/2} - \frac{1}{2} T_{(i-1)j} R_{(i-1)j}^{-3/2} R_{(i-1)j,i} \\ &= \frac{1}{4} (x_{j+1} - x_j) R_{(i-1)j}^{-1/2} - \frac{1}{4} T_{(i-1)j} R_{(i-1)j}^{-3/2} (x_i + x_{i-1} - x_{j+1} - x_j) \end{aligned}$$

Otherwise, there are two special terms where multiple presence of x_i causes the derivative to behave differently. These are when $j = i-1$, or

$$\begin{aligned} h_{i(i-1),i} &= T_{i(i-1),i} R_{i(i-1)}^{-1/2} + T_{i(i-1)}(R_{i(i-1)}^{-1/2})_{,i} \\ &= T_{i(i-1),i} R_{i(i-1)}^{-1/2} - \frac{1}{2} T_{i(i-1)} R_{i(i-1)}^{-3/2} R_{i(i-1),i} \\ &= \frac{1}{4} R_{i(i-1)}^{-1/2} (x_{i+1} + x_{i-1} - 2x_i) \end{aligned}$$

and when $j = i+1$, or

$$\begin{aligned} h_{i(i+1),i} &= T_{i(i+1),i} R_{i(i+1)}^{-1/2} + T_{i(i+1)}(R_{i(i+1)}^{-1/2})_{,i} \\ &= T_{i(i+1),i} R_{i(i+1)}^{-1/2} - \frac{1}{2} T_{i(i+1)} R_{i(i+1)}^{-3/2} R_{i(i+1),i} \\ &= \frac{1}{4} R_{i(i+1)}^{-1/2} (x_{i+1} - x_{i+2}) - \frac{1}{4} T_{i(i+1)} R_{i(i+1)}^{-3/2} (x_i - x_{i+2}) \end{aligned}$$

Only nonzero terms of the gradient are shown here. To get the gradient of \mathcal{L} with respect to a given variable, simply sum the contributions of the gradient of each component term. Derivatives with respect to x_k are shown in lieu of ones with respect to y_k if the formulae are symmetric in those variables. For F_μ , we have

$$\begin{aligned} \frac{\partial F_\mu}{\partial x_k} &= -\frac{1}{2} \sum_{i=1}^N \sum_{\substack{j=1 \\ j \neq i}}^N h_{ij,k} \\ &= -\frac{1}{2} \left[\sum_{\substack{j=1 \\ j \neq k, k-1, k+1}}^N h_{kj,k} + \sum_{\substack{j=1 \\ j \neq k-1, k}}^N h_{(k-1)j,k} + h_{k(k-1),k} + h_{k(k+1),k} \right] \end{aligned}$$

For the constraints, we have

$$\frac{\partial C_{\text{dist}}}{\partial x_k} = 2 [\lambda_k (x_{k+1} - x_k) - \lambda_{k-1} (x_k - x_{k-1})]$$

$$\frac{\partial C_A}{\partial x_k} = \frac{1}{2}\lambda_A(y_{k-1} - y_{k+1}) \quad \frac{\partial C_A}{\partial y_k} = \frac{1}{2}\lambda_A(x_{k+1} - x_{k-1})$$

$$\frac{\partial C_x}{\partial x_k} = \lambda_x \quad \frac{\partial C_y}{\partial y_k} = \lambda_y$$

F_L only depends on the perimeter L , and its gradient contribution is

$$\frac{\partial F_L}{\partial L} = \Lambda + H_{\frac{N-1}{2}} - \log L - 1$$

The only constraint with L dependence is C_{dist} , and it yields

$$\frac{\partial C_{\text{dist}}}{\partial L} = 2\frac{L}{N^2} \sum_{i=1}^N \lambda_i$$

The derivative of any constraint term with respect to its Lagrange multiplier simply yields the expression of that constraint, or

$$\frac{\partial C_A}{\partial \lambda_A} = \pi - \frac{1}{2} \sum_{i=1}^N (x_i y_{i+1} - x_{i+1} y_i) \quad \frac{\partial C_{\text{dist}}}{\partial \lambda_i} = \frac{L^2}{N^2} - \|\vec{x}_{i+1} - \vec{x}_i\|^2$$

$$\frac{\partial C_x}{\partial \lambda_x} = \sum_{i=1}^N x_i \quad \frac{\partial C_y}{\partial \lambda_y} = \sum_{i=1}^N y_i$$

These are all the nonzero terms of the gradient of our Lagrangian in the absence of an external potential. A similar analysis can be done to recover terms for the external potential and for the Hessian, albeit a lengthy one.

APPENDIX C

MODIFIED LEVENBERG–MARQUARDT

The following is the C++ header file for the core algorithm in our library. The reason it is a header file is that we wish to use this algorithm with a variety of Hessian matrices, e.g., the vanilla Hessian, the random background Hessian, the fixed point Hessian, etc. Therefore, we make use of templates to hand this function unspecified energy, gradient, and Hessian functions, which we can later insert in other code. This code is released under the GPL, whose license is available at <https://www.gnu.org/licenses/gpl-3.0.txt>. It and all other libraries and methods used in this thesis can be found at <https://github.com/kentdobias/dipole>.

domain_newton.h

```

1  #ifndef DOMAIN_NEWTON_H
   #define DOMAIN_NEWTON_H
   #include <math.h>
   #include <iostream>
6  #include <string>
   // GSL includes.
   #include <gsl/gsl_math.h>
   #include <gsl/gsl_vector.h>
11  #include <gsl/gsl_blas.h>
   #include <gsl/gsl_sf.h>
   // Eigen's linear solving uses cheap parallelization.
   #include <eigen3/Eigen/Dense>
16
   /* This function is templated so that any set of functions which return an
   * energy, gradient, and Hessian given an empty object, the size of the state
   * vector, and the state vector can be used. This allows many such sets of
   * functions, e.g., that for a fixed domain or a domain on a random background,
21  * to be used. See the file domain_minimize.cpp for examples of construction
   * of these functions.
   */
   template <class energy_func, class grad_func, class hess_func>
26  int domain_newton(gsl_vector *state, unsigned size, unsigned params,
   energy_func get_energy, grad_func get_grad, hess_func get_hess, double
   epsilon, unsigned max_iterations, double beta, double s, double sigma,
   double gamma, double eta_0, double delta, double bound, bool verbose, bool
   save_states) {
31  /* The function domain_newton carries out a modified version of Newton's
   * method. On success, 0 is returned. On failure, 1 is returned.
   *
   * state          - GSL_VECTOR
   *                On entry, state gives the system's initial condition. On
36  *                exit, state contains the result Newton's method.
   *
   * size           - UNSIGNED INTEGER
   *                On entry, size gives the size of the vector state. Unchanged
41  *                on exit.
   *
   * params         - UNSIGNED INTEGER
   *                On entry, params gives the number of non-multiplier elements

```

```

*          in state, which are assumed by the function to be the first
*          elements of state.  Unchanged on exit.
46 *
* get_energy - ENERGY_FUNC
*          On entry, get_energy is a function that returns a double
*          float.  The first argument of get_energy is an unsigned
*          integer and the second argument is a gsl_vector object.  This
51 *          function is expected to take size and state, respectively,
*          and return the energy of that state.  Unchanged on exit.
*
* get_grad - GRAD_FUNC
*          On entry, get_grad is a function that returns void.  The
56 *          first argument of get_grad is a gsl_vector object, the second
*          argument of get_grad is an unsigned integer, and the third
*          argument of get_grad is a gsl_vector object.  This function
*          is expected to take a vector of size size, size, and state,
*          respectively.  It leaves the gradient of the energy function
61 *          in the first argument.  Unchanged on exit.
*
* get_hess - HESS_FUNC
*          On entry, get_hess is a function that returns void.  The
*          first argument of get_hess is a gsl_matrix object, the second
66 *          argument of get_hess is an unsigned integer, and the third
*          argument of get_hess is a gsl_vector object.  This function
*          is expected to take a matrix of size size by size, size, and
*          state, respectively.  It leaves the Hessian of the energy
*          function in the first argument.  Unchanged on exit.
71 *
* epsilon - DOUBLE FLOAT
*          On entry, epsilon gives the number that is used to judge
*          convergence.  When the norm of the gradient is less than
*          epsilon * size, the process is deemed complete and the
76 *          iterations are stopped.  Unchanged on exit.
*
* max_iterations - UNSIGNED INTEGER
*          On entry, max_iterations gives the maximum number of times
*          the algorithm will repeat before failing.  Unchanged on exit.
81 *
* beta - DOUBLE FLOAT
*          On entry, beta gives the number which is exponentiated to
*          scale the step size in Newton's method.  Unchanged on exit.
*
86 * s - DOUBLE FLOAT
*          On entry, s gives a constant scaling of the step size in
*          Newton's method.  Unchanged on exit.
*
* sigma - DOUBLE FLOAT
91 *          On entry, sigma gives a scaling to the condition on the step
*          size in Newton's method.  Unchanged on exit.
*
* gamma - DOUBLE FLOAT
*          On entry, gamma gives the amount by which the norm of the
96 *          gradient must change for eta to decrement by a factor delta.
*          Unchanged on exit.
*
* eta_0 - DOUBLE FLOAT
101 *          On entry, eta_0 gives the starting value of eta.  Unchanged
*          on exit.
*
* delta - DOUBLE FLOAT
*          On entry, delta gives the factor by which eta is decremented.
106 *          Unchanged on exit.
*
* bound - DOUBLE FLOAT
*          On entry, delta gives an upper bound to the gradient norm.
*          If surpassed, the execution is halted and the program returns
*          failure.  Unchanged on exit.
111 *
* verbose - BOOLEAN
*          On entry, verbose indicates whether verbose output will be
*          printed to stdout by this program.  Unchanged on exit.
*/
116
// Declaring variables.
double ratio, norm, old_norm, old_energy, energy, grad_dz_prod, alpha, eta;
unsigned iterations, m;
bool converged, bound_exceeded;
121

```

```

// Declaring GSL variables.
gsl_vector *grad, *dz;
gsl_matrix *hess;

126 // Allocating memory for GSL objects
grad = gsl_vector_alloc(size);
dz = gsl_vector_alloc(size);
hess = gsl_matrix_alloc(size, size);

131 // Declaring Eigen map objects to wrap the GSL ones.
Eigen::Map<Eigen::VectorXd> grad_eigen(grad->data, size);
Eigen::Map<Eigen::VectorXd> dz_eigen(dz->data, size);
Eigen::Map<Eigen::MatrixXd> hess_eigen(hess->data, size, size);

136 // If epsilon > 0, use its value. Otherwise, set to machine precision.
if (epsilon == 0) epsilon = DBL_EPSILON;

// Initializes the starting value of old_norm at effectively infinity.
141 old_norm = 1 / DBL_EPSILON;

// Start the loop parameter at zero.
iterations = 0;

/* If the loop ends and this boolean has not been flipped, the program will
* know it has not converged.
*/
converged = false;

// Initializes the value of eta.
151 eta = eta_0;

// Begins the algorithm's loop.
while (iterations < max_iterations) {

156 // Gets the energy, gradient and Hessian for this iteration.
old_energy = get_energy(size, state);
get_grad(grad, size, state);
get_hess(hess, size, state);

161 // Adds eta along the diagonal of the Hessian for non-multiplier entries.
for (unsigned i = 0; i < params; i++) {
    gsl_matrix_set(hess, i, i, gsl_matrix_get(hess, i, i) + eta);
}

166 // Use LU decomposition to solve for the next step in Newton's method.
dz_eigen = hess_eigen.lu().solve(grad_eigen);

// Dots the gradient into the step in order to judge the step size.
171 gsl_blas_ddot(grad, dz, &grad_dz_prod);

// Initializes the Armijo counter.
m = 0;

// This loop determines the Armijo step size.
176 while (true) {
    alpha = gsl_sf_pow_int(beta, m) * s;
    gsl_vector_scale(dz, alpha);
    gsl_vector_sub(state, dz);

181    energy = get_energy(size, state);

    if (fabs(old_energy - energy) >= sigma * alpha * grad_dz_prod) break;
    else {
        gsl_vector_add(state, dz);
186        gsl_vector_scale(dz, 1 / alpha);
        m++;
    }
}

191 // Gets the new norm of the gradient for comparison.
norm = gsl_blas_dnorm2(grad) / size;

// Judges if the norm has changed sufficiently little to decrement eta.
196 if (fabs(norm - old_norm) < gamma * eta) eta *= delta;

// Prints several useful statistics for debugging purposes.
if (verbose) printf("NEWTON_STEP%06d: %i, %g, %e, %e\n",
    iterations, m, norm, eta, energy);

```

```
201     // Determines if the process has converged to acceptable precision.
    if (norm < epsilon) {
        converged = true;
        break;
    }
206     // Causes the program to fail if norm has diverged to a large number.
    if (norm > bound) break;

    // Reset the norm for the next iteration.
211     old_norm = norm;

    if (save_states) {
        char str[40];
        sprintf(str, "states/state-%06d.dat", iterations);
216         FILE *fout = fopen(str, "w");
        gsl_vector_fprintf(fout, state, "%.15e");
        fclose(fout);
    }

    // Increment the counter.
221     iterations++;
    }

    // Gotta live free, die hard. No one likes memory leaks.
226     gsl_vector_free(grad);
    gsl_vector_free(dz);
    gsl_matrix_free(hess);

    // Return conditions to indicate success or failure.
231     if (converged) return 0;
    else return 1;
}

#endif
```


BIBLIOGRAPHY

- [1] J. C. Alexander, A. J. Bernoff, E. K. Mann, J. A. Mann, J. R. Wintersmith, and L. Zou. Domain relaxation in Langmuir films. *Journal of Fluid Mechanics*, 571:191–220, 2007.
- [2] D. P. Bertsekas. *Nonlinear Programming*. Athena Scientific, Belmont, MA, 2nd edition, 1999.
- [3] R. de Koker, W. Jiang, and H. M. McConnell. Instabilities of the stripe phase in lipid monolayers. *The Journal of Physical Chemistry*, 99(16):6251–6257, 1995.
- [4] R. de Koker and H. M. McConnell. Circle to dogbone: shapes and shape transitions of lipid monolayer domains. *The Journal of Physical Chemistry*, 97(50):13419–13424, 1993.
- [5] R. de Koker and H. M. McConnell. Shape transitions of lipid monolayer domains in an external field. *The Journal of Physical Chemistry*, 98(20):5389–5393, 1994.
- [6] J. Deutch and F. Low. Theory of shape transitions of two-dimensional domains. *The Journal of Physical Chemistry*, 96(17):7097–7101, 1992.
- [7] A. J. Dickstein, S. Erramilli, R. E. Goldstein, D. P. Jackson, and S. A. Langer. Labyrinthine pattern formation in magnetic fluids. *Science*, 261(5124):1012–1015, 1993.
- [8] M. P. Do Carmo. *Differential Geometry of Curves and Surfaces*. Pearson, London, GB, 1976.
- [9] P. L. Edmiston, J. E. Lee, L. L. Wood, and S. S. Saavedra. Dipole orientation distributions in Langmuir—Blodgett films by planar waveguide linear dichroism and fluorescence anisotropy. *The Journal of Physical Chemistry*, 100(2):775–784, 1996.
- [10] F. Elias, C. Flament, J.-C. Bacri, and S. Neveu. Macro-organized patterns in ferrofluid layer: Experimental studies. *Journal de Physique I*, 7(5):711–728, 1997.
- [11] C. Flament, G. Pacitto, J.-C. Bacri, I. Drikis, and A. Cebers. Viscous fingering in a magnetic fluid. I. Radial Hele-Shaw flow. *Physics of Fluids*, 10(10):2464–2472, 1998.
- [12] D. Gallez and H. M. McConnell. Coupling of size and shape equilibration in lipid monolayer domains. *The Journal of Physical Chemistry B*, 104(7):1657–1662, 2000.

- [13] R. E. Goldstein and D. P. Jackson. Domain shape relaxation and the spectrum of thermal fluctuations in Langmuir monolayers. *The Journal of Physical Chemistry*, 98(38):9626–9636, 1994.
- [14] P. Guyot-Sionnest, J. Hunt, and Y. Shen. Sum-frequency vibrational spectroscopy of a Langmuir film: Study of molecular orientation of a two-dimensional system. *Physical Review Letters*, 59(14):1597, 1987.
- [15] J.-P. Hansen and I. R. McDonald. *Theory of simple liquids*. Elsevier, 1990.
- [16] P. Heinig, L. Helseth, and T. M. Fischer. Relaxation of patterns in 2D modulated phases. *New Journal of Physics*, 6(1):189, 2004.
- [17] N. J. Hillier and D. P. Jackson. Width of a ferrofluid finger: Hysteresis and a double energy minimum. *Physical Review E*, 75(3):036314, 2007.
- [18] D. P. Jackson. Hysteresis and multiple stable configurations in a magnetic fluid system. *Journal of Physics: Condensed Matter*, 20(20):204140, 2008.
- [19] D. P. Jackson, R. E. Goldstein, and A. O. Cebers. Hydrodynamics of fingering instabilities in dipolar fluids. *Physical Review E*, 50(1):298, 1994.
- [20] Z. Khattari and T. M. Fischer. Shapes of Langmuir monolayer domains in confined geometries. *The Journal of Physical Chemistry B*, 106(7):1677–1683, 2002.
- [21] L. D. Landau and E. M. Lifshitz. *Statistical Physics Part 1*. Elsevier Ltd., Burlington, MA, 3rd edition, 1980.
- [22] S. A. Langer, R. E. Goldstein, and D. P. Jackson. Dynamics of labyrinthine pattern formation in magnetic fluids. *Physical Review A*, 46(8):4894, 1992.
- [23] D. K. Lubensky and R. E. Goldstein. Hydrodynamics of monolayer domains at the air–water interface. *Physics of Fluids (1994-present)*, 8(4):843–854, 1996.
- [24] E. Mann and S. Primak. Stability of two-dimensional foams in Langmuir monolayers. *Physical Review Letters*, 83(25):5397, 1999.
- [25] H. M. McConnell. Harmonic shape transitions in lipid monolayer domains. *Journal of Physical Chemistry*, 94(11):4728–4731, 1990.
- [26] H. M. McConnell and R. de Koker. Note on the theory of the sizes and shapes of lipid domains in monolayers. *The Journal of Physical Chemistry*, 96(17):7101–7103, 1992.
- [27] H. M. McConnell and R. de Koker. Equilibrium thermodynamics of lipid monolayer domains. *Langmuir*, 12(20):4897–4904, 1996.
- [28] H. M. McConnell and V. T. Moy. Shapes of finite two-dimensional lipid domains. *The Journal of Physical Chemistry*, 92(15):4520–4525, 1988.

- [29] A. Mulero, editor. *Theory and Simulation of Hard-Sphere Fluids and Related Systems*. Springer, New York, NY, 2008.
- [30] F. Otto. Dynamics of labyrinthine pattern formation in magnetic fluids: A mean-field theory. *Archive for Rational Mechanics and Analysis*, 141(1):63–103, 1998.
- [31] M. Seul and D. Andelman. Domain shapes and patterns: the phenomenology of modulated phases. *Science*, 267(5197):476–483, 1995.
- [32] M. Seul, L. Monar, L. O’Gorman, and R. Wolfe. Morphology and local structure in labyrinthine stripe domain phase. *Science*, 254(5038):1616–1618, 1991.
- [33] H. Stone and H. McConnell. Hydrodynamics of quantized shape transitions of lipid domains. *Proceedings of the Royal Society of London. Series A: Mathematical and Physical Sciences*, 448(1932):97–111, 1995.
- [34] G. Tucker. Formation of labyrinth patterns in Langmuir films. 2008.
- [35] J. Umemura, T. Kamata, T. Kawai, and T. Takenaka. Quantitative evaluation of molecular orientation in thin Langmuir-Blodgett films by FT-IR transmission and reflection-absorption spectroscopy. *The Journal of Physical Chemistry*, 94(1):62–67, 1990.
- [36] T. Vanderlick and H. Moehwald. Mode selection and shape transitions of phospholipid monolayer domains. *Journal of Physical Chemistry*, 94(2):886–890, 1990.
- [37] J. R. Wintersmith, L. Zou, A. J. Bernoff, J. C. Alexander, J. A. Mann Jr, E. E. Kooijman, and E. K. Mann. Determination of interphase line tension in Langmuir films. *Physical Review E*, 75(6):061605, 2007.
- [38] J. Yarnell, M. Katz, R. G. Wenzel, and S. Koenig. Structure factor and radial distribution function for liquid argon at 85 K. *Physical Review A*, 7(6):2130, 1973.
- [39] T. Zhang, C. Zhang, and G. Wong. Determination of molecular orientation in molecular monolayers by second-harmonic generation. *JOSA B*, 7(6):902–907, 1990.